Title: Oxygen isotope ratios in zircon and garnet: A record assimilation and fractional crystallization in the Dinkey Dome peraluminous granite, Sierra Nevada, CA

Manuscript Number: 7472

Authors: Raiza Quintero, Curtin University Kouki Kitajima, University of Wisconsin-Madison Reinhard Kozdon, Lamont-Doherty Earth Observatory Ariel Strickland, Univ. Wisconsin Jade Star Lackey, Pomona College John Valley, University of Wisconsin - Madison

# Oxygen isotope ratios in zircon and garnet: A record assimilation and fractional crystallization in the Dinkey Dome peraluminous granite, Sierra Nevada, CA

Raiza R. Quintero[1*], Kouki Kitajima[1], Reinhard Kozdon[1,2], Ariel Strickland[1], Jade Star Lackey[3], and John W. Valley[1]

[1]WiscSIMS, Department of Geoscience, University of Wisconsin, Madison, WI, 53706, USA

[2]Lamont-Doherty Earth Observatory of Columbia University, Palisades, NY, 10964, USA

[3]Geology Department, Pomona College Claremont, CA, 91711, USA

Final Publication:
Quintero RR, Kitajima K, Kozdon R, Strickland A, Lackey J-S and Valley JW (2021) Oxygen isotope ratios in zircon and garnet: A record assimilation and fractional crystallization in the Dinkey Dome peraluminous granite, Sierra Nevada, CA. Am. Mineral. 106: 715-729. doi.org/10.2138/am-2021-7472

*Corresponding Author present address:

Space Science Technology Centre, School of Earth and Planetary Science, Curtin University of Technology GPO Box U1987, Perth, WA, 6845

Australiar.quinteromendez@postgrad.curtin.edu.au

## Abstract

The 119 Ma Dinkey Dome pluton in the central Sierra Nevada Batholith is a peraluminous granite and contains magmatic garnet and zircon with complexly zoned oxygen isotope ratios. Intracrystalline SIMS analysis tests the relative importance of magmatic differentiation processes vs. partial melting of metasedimentary rocks. Whereas $\delta^{18}O$ values of bulk zircon concentrates are uniform across the entire pluton (7.7‰ VSMOW), zircon crystals are zoned in $\delta^{18}O$ by up to 1.8‰, and when compared to late garnet, shows evidence of changing magma chemistry during multiple interactions of the magma with wall rock during crustal transit. The evolution from an early high-$\delta^{18}O$ magma [$\delta^{18}O$(WR) = 9.8‰] towards lower values is shown by high $\delta^{18}O$ zircon cores (7.8‰) and lower $\delta^{18}O$ rims (6.8‰). Garnets from the northwest side of the pluton show a final increase in $\delta^{18}O$ with rims reaching 8.1‰. In situ REE measurements show zircon is magmatic and grew before garnets. Additionally, $\delta^{18}O$ in garnets from the eastern side of the pluton are consistently lower (Ave = 7.3‰) relative to the east (Ave = 5.9‰).

These $\delta^{18}O$ variations in zircon and garnet record different stages of assimilation and fractional crystallization whereby an initially high $\delta^{18}O$ magma partially melted low $\delta^{18}O$ wallrock and was subsequently contaminated near the current level of emplacement by higher $\delta^{18}O$ melts. Collectively, the comparison of $\delta^{18}O$ zoning in garnet and zircon shows how a peraluminous pluton can be constructed from multiple batches of variably contaminated melts, especially in early stages of arc magmatism where magmas encounter significant heterogeneity of wall-rock assemblages. Collectively, peraluminous magmas in the Sierran arc are limited to small < 100 km$^2$ plutons that are intimately associated with metasedimentary wallrocks and often surrounded by later and larger, metaluminous tonalite and granodiorite plutons. The general

associations suggest that early stage arc magmas sample crustal heterogeneities in small melt batches, but that with progressive invigoration of the arc, such compositions are more effectively blended with mantle melts in source regions. Thus, peraluminous magmas provide important details of the nascent Sierran arc and pre-batholithic crustal structure.

***Keywords:*** peraluminous granite, garnet, zircon, Sierra Nevada, oxygen isotopes, REE, SIMS

## Introduction

The petrogenesis of peraluminous granites is a longstanding question (Clemens and Wall 1981; Patiño Douce and Johnston 1991; Frost et al. 2001; Villaros et al. 2009; Lackey et al. 2011). Peraluminous composition in granitoid rocks is defined by molar proportions of $Al_2O_3$ in excess of combined CaO, $Na_2O$, and $K_2O$: $Al_2O_3/(CaO+K_2O+Na_2O) > 1$, or an aluminum saturation index (ASI > 1; Zen 1988). Peraluminous granitoids typically form from a high proportion of melts of aluminous crustal or sedimentary source rocks (Chappell and White 1974; Scaillet et al. 2016). Alternative mechanisms can explain the generation of weakly peraluminous compositions in granitoid rocks (e.g. fractional crystallization, crustal anatexis and vapor phase transfer; Zen 1988).

Isotope tracers can discriminate between source, magmatic differentiation, and contamination characteristics of peraluminous magmas. Early work showed correlated $^{87}Sr/^{86}Sr$ and $\delta^{18}O$ as indicative of crustal melting (O'Neil and Chappell 1977; Halliday et al. 1981). Oxygen isotope ratios are affected by assimilation of crustal rocks, which have different $\delta^{18}O$ values than mantle-derived magmas (e.g., Taylor and Sheppard 1986; Valley et al. 2005). In cases where crustal melts are produced from young source rocks, radiogenic isotopes are not sensitive, and oxygen isotopes are typically the most sensitive isotopic tracer (e.g., Valley 2003; Lackey et al. 2011; Jeon et al. 2012).

Oxygen isotopes can be measured in retentive zoned minerals to record information about magma evolution (e.g., Valley 2003; Bindeman 2008; Lackey et al. 2011). Self-diffusion rates of oxygen in garnet and zircon are among the slowest in common minerals (Coughlan 1990; Wright et al. 1995; Watson and Cherniak 1997; Vielzeuf et al. 2005; Page et al. 2007b, 2010; Bowman et al. 2011), and crystallization of both minerals in peraluminous granites allows them to be used in tandem to record a more complete tine history than would be provided by a single mineral (Lackey et al. 2011). The $\delta^{18}O$ values of zircon and garnet are quenched upon crystallization and growth zoning provides a record of magmatic evolution (King and Valley 2001; Valley 2003; Lackey et al. 2006).

Zircon and other accessory minerals also record the rare earth element (REE) compositions of felsic magmas during their growth (Sawka and Chappell 1988; Hoskin et al. 2000; Hoskin and Schaltegger 2003). Rare earths are incorporated in zircon by coupled substitution mechanisms (Speer 1982; Hinton and Upton 1991; Halden et al. 1993; Hoskin and Ireland 2000; Finch et al. 2001; Hoskin and Schaltegger 2003).

In this study, we employ secondary ion mass spectrometry (SIMS) to measure oxygen isotope ratios ($\delta^{18}O$) and trace element compositions, including Y + REEs. The SIMS method provided accurate and precise measurements of intracrystalline zoning at high spatial resolution (ca. 10 µm) in zircon and garnet crystals collected throughout the Dinkey Dome granite (Fig. 1). The zoning measured within these crystals is evident in multiple proxies and is useful to contextualize contamination, assimilation, and/or high temperature alteration processes during growth of both zircon and garnet.

The resulting data constrain models for the origin and contamination of silicic melts in the Sierra Nevada batholith. The processes that formed this and other granites senso stricto in the

Sierra are critical to understand the relative contribution of preexisting crust in the Sierran arc and evaluate the different processes that affected the composition and final magmas.

## Geology

### The Sierra Nevada Batholith

The voluminous Cretaceous Sierra Nevada batholith, California (Fig. 1) consists mainly of tonalite to granodiorite plutons to depths ~35 km (Saleeby et al. 2003), with more mafic diorite and refractory gabbroic residues continuing to ca. 45 km (Fliedner et al. 2000). Gabbro complexes, and mafic enclaves are a common but volumetrically small part of the batholith and have been targeted to study the mass balance of mantle and crustal melt inputs to produce the intermediate, granodiorite compositions that are the bulk of the batholith (Dorais et al. 1990; Coleman et al. 1997; Wenner and Coleman 2004). Other studies have examined the sub-arc mantle and residual mafic root of the batholith, sampled as pyroxenite, garnet-clinopyroxenite, and lherzolite xenoliths in Cenozoic volcanic rocks (Moore and Dodge 1980; Ducea 2001; Lee et al. 2006; Chin et al. 2014). Such studies provide additional information on mantle controls of magmatic heat budgets and mafic magma flux, revealing in detail that multi-stage crystallization and re-melting episodes are required to build granodioritic crust that complements the major element (e.g., Mg) and isotopic compositions of xenoliths. In addition, experimental studies show that high silica melts can be produced from re-melting of Sierran gabbros (Sisson et al. 2005; Ratajeski et al. 2005)

Despite considerable attention to magmatic origins recorded in mafic to ultramafic rocks, few studies have focused on potential high-silica melts; $\delta^{18}O$ studies of granodiorite and tonalite suites require at least 15-30% input of melts from supracrustal sources, thus partial melting of gabbros is not the sole source of potential high-silica end-member melts. Thus, direct studies of rocks with relatively undiluted high-silica crustal melts are important, but only a handful have been undertaken: Wenner and Coleman (2004) studied several granites in a regional survey of both mafic and felsic plutons in the Sierra; Zeng et al. (2005) examined partial melting in a lower crustal migmatite complex in the Southern Sierra Nevada; Lackey et al. (2006) studied regional and pluton-scale patterns of $\delta^{18}O$ of peraluminous granites in the Sierra. These three studies found evidence of crustal melting in the granitic plutons and migmatites, highlighting the importance of such melts as a factor in the isotopic variability in many Sierran granodiorites, hence, added motivation to study the Dinkey Dome granite.

**The Dinkey Dome Granite**

The garnet, two-mica Dinkey Dome granite is a relatively small (~30 km$^2$) pluton surrounded by granodiorite plutons (e.g., Dinkey Creek Granodiorite) and other granites of the Shaver Intrusive Suite (Figs. 1 and 2; Bateman 1992; Lackey et al. 2006). With a U-Pb zircon age of 119 Ma (Frazer et al. 2008), the Dinkey Dome pluton is coeval with the oldest members of the Fine Gold Intrusive Suite to the west, and significantly older than other members of the Shaver Intrusive Suite (Frazer et al. 2008). Thus, the Dinkey Dome represents a case of magmatism that was anomalously inboard of the broad magmatic “locus” in the Sierra at the time it was emplaced, and a departure from the broad trend of eastward-younging Cretaceous intrusive suites in the Sierran Arc (Chen and Moore 1982; Memeti et al. 2010; Davis et al. 2012; Lackey et al. 2012; Ardill et al. 2018; Chapman and Ducea 2019). Initial $^{87}Sr/^{86}Sr$ ratios of the Dinkey Dome granite are 0.7065 (Kistler and Peterman 1973). Metamorphic wallrocks consist of quartzite, mica schist, biotite hornfels, and marble (Fig. 2) (Bateman and Wones 1972). The chemistry of the pluton and aluminous minerals (garnet, muscovite, $Al_2SiO_5$) contained therein are typical for peraluminous granites. Whole rock geochemical analyses of the Dinkey Dome show that aluminum saturation indices (ASI) are peraluminous (west side ASI = 1.02; east side ASI = 1.07; Lackey et al. 2006). Average garnet compositions in the Dinkey Dome granite are $Alm_{72.4}Sps_{19.5}Pyp_{5.8}Grs_{2.3}$ on the west and $Alm_{78.6}Sps_{19.1}Pyp_{0.9}Grs_{1.4}$ on the east. There are no garnet-bearing metamorphic wallrocks in contact with the Dinkey Dome, consistent with the magmatic origin of garnet (Lackey et al. 2011). Shallow crystallization is inferred by scattered miarolitic cavities in the east side of the pluton that are inferred to indicate a pressure of <1 kbar (Wones et al. 1969). In contrast, the Dinkey Creek Granodiorite, which engulfs the Dinkey Dome pluton and other surrounding Dinkey Dome type granites, has Al-in-hornblende pressure estimates of 4.0 ±0.4 kbar for 10 widely distributed samples reported by Tobisch et al. (1993) who recalculated values from data reported by Ague and Brimhall (1988b). Although crystallization of Dinkey Creek hornblende at the current level of emplacement is not certain, if the Dinkey Dome granite is ~8 million years older than the Dinkey Creek Granodiorite (Frazer et al. 2008), the pressure/age differential implies 10 km of burial of the Dinkey Dome granite and its pendant rocks in 8 million years.

Construction of younger batholith with higher apparent pressures around pendants and older plutons that are relatively shallow is seen elsewhere in the Sierra Nevada. For instance, recent oxygen isotope analysis of skarn garnets in the Mineral King pendant shows paleo-hydrothermal systems were infiltrated by surface-derived fluids at ca. 135 Ma (Ryan-Davis et al. 2019) and again at ca. 109 Ma (D'Errico et al. 2012), but that younger (98 Ma) voluminous granodiorite plutons that surrounds the pendant and these hydrothermal systems record apparent emplacement pressures of ca. 3 kbar (Ague and Brimhall 1988b), well below the possible brittle-ductile transition depth that would permit extensive meteoric water circulation. Similarly, volcanic rocks with steep, down-dip stretching lineations are often found adjacent to slightly younger plutonic rocks (Tobisch et al. 2000). This juxtaposition of older, near surface against higher pressure, younger plutons suggests that the older rocks were engulfed by later magmas as the batholith is built upward around them through interplays of bulk arc thickening, structural shortening, or density driven return flow (e.g., Saleeby et al. 2003).

## Previous Isotopic Work

Lackey et al. (2006) analyzed $\delta^{18}O$ by laser fluorination of garnet (Grt), zircon (Zrn), quartz (Qz), Andalusite (And) and whole rock powders (WR) in the Dinkey Dome pluton (Fig. 2) as part of a regional study of peraluminous granitoid plutons in the Sierra Nevada. This study produced several key results. First, values of $\delta^{18}O$ are elevated: $\delta^{18}O$(WR) = 9.6–10.4‰ VSMOW, $\delta^{18}O$(Qz)= 10.6–11.3‰, $\delta^{18}O$(And)= 8.4–8.5‰, $\delta^{18}O$(Zrn)= 7.0–7.8‰, and $\delta^{18}O$(Grt)= 6.7–7.4‰. The surrounding Kings Sequence metasedimentary rocks (marbles, hornfels, and quartzites) of the Dinkey Creek pendant have $\delta^{18}O$(WR) of 9.5–11.6‰. Other peraluminous granites in the Sierra Nevada Batholith also have high $\delta^{18}O$(Zrn) >7.5‰, while metaluminous granitic rocks near the Dinkey Dome have average zircon $\delta^{18}O$ values that range from 6.5–7.5‰ (Lackey et al. 2006, 2008).

Values of $\delta^{18}O$ for zircon, quartz and whole rock are unimodal across the entire pluton, however, $\delta^{18}O$ values of magmatic garnet are bimodal, decreasing by ~0.6‰ on the east side of the central metasedimentary septum within the Dinkey Dome (Fig. 2). High $\delta^{18}O$ values and equilibrium fractionations of garnet and zircon on the west side of the pluton ($\Delta^{18}O$(Grt-Zrn) = 0.06 ±0.13‰), indicate that prior to the crystallization of both minerals, the magma was elevated in $\delta^{18}O$. On the eastern side, $\delta^{18}O$ values of garnet are lower and not equilibrated with zircon ($\Delta^{18}O$ (Grt-Zrn) = –0.6 ±0.13‰), recording a change in magmatic $\delta^{18}O$ synchronous with crystallization. These differences in fractionation are small but distinct. The lower $\delta^{18}O$ values in garnet that formed later than zircons, seen as inclusions in garnet (Figs. 3c and d), suggest that low $\delta^{18}O$ material was assimilated after the crystallization of zircon and before crystallization of garnet. These results are interpreted to indicate that the Dinkey Dome granitic magmas evolved through contamination by low $\delta^{18}O$ material, however no low $\delta^{18}O$ country rocks are exposed in the Dinkey Creek Pendant. Thus, partial melting by of such a low $\delta^{18}O$ contaminant would be required to have occurred deeper in the crust (Lackey et al. 2006).

# Methods

## Sample Preparation and Imaging

Zircon and garnet mineral separates of ten samples from Lackey et al. (2006) (samples 1S51 to 1S82) were handpicked and cast in 25-mm diameter round epoxy mounts along with the Kim-5 zircon (Valley 2003) and UWG-2 garnet (Valley et al. 1995) standards, ground to the level of best mineral exposure, polished to a smooth, flat, low-relief surface, and carbon coated prior to imaging. Secondary Electron (SE), Backscattered Electron (BSE) and Cathodoluminescence (CL) images were obtained for each grain, and Energy Dispersive X-ray Spectrometry (EDS) was conducted using the UW-Madison, Dept. of Geoscience Hitachi S-3400N SEM (Scanning Electron Microscope). Based on the images obtained, approximately 10 zircon grains (that display distinctive rims and cores) and five garnet grains were chosen for in situ analysis from each sample. The SEM images were also used to locate the positions for SIMS analyses. Carbon coats were then removed and the mounts were coated with gold for SIMS analysis.

Twenty-five-mm round thin sections were made of samples collected during this study (samples 10DD02-10DD19, Table 1, Supplementary Table A) (Fig. 2) and top mounted with UWQ-1 quartz standard (Kelly et al. 2007) and UWG-2 in their centers. Isotopic analysis of minerals in thin section rather than in grain mounts permits detailed descriptions of zircon and garnet that are in known petrographic relation to each other. Imaging prior to SIMS analysis was conducted in the same manner as described above.

**Major and minor element analyses of garnet by electron microprobe**

Determination of composition and testing for compositional zoning preceded every SIMS $\delta^{18}O$ analysis of garnet. Major and minor element analyses of garnet were obtained using the UW-Madison, Dept. of Geoscience CAMECA SX51 electron microprobe by wavelength dispersive spectrometry. Eight elements were analyzed: Si, Al, Fe, Mg, Mn, Ca, Ti, and Cr (Supplementary Table B). The operating conditions were accelerating potential of 15KeV, 40° takeoff angle, and a fixed focused beam at 20 nA. Counting time for all elements was 10 seconds on-peak and 10 seconds off-peak. LIF, PET, and TAP analyzer crystals were used to acquire Kα X-ray intensities for Mn, Fe and Cr; Ca and Ti; and Al, Si and Mg, respectively. Crystalline standards were used: Minas Gerais rutile for Ti; U.W. synthetic fayalite for Fe; synthetic tephroite for Mn; USNM 143968 Kakanui pyrope for Mg; $Andradite_{99}$-Rota (Hungary) for Ca; synthetic $Cr_2O_3$ for Cr; and HU $Almandine_{56}$ for Al and Si.

**Laser Fluorination analysis of $\delta^{18}O$**

In order to assess any correlation of chemical composition with $\delta^{18}O$, individual garnet grains (~1.5-2.0 mg) from 10 samples previously studied by Lackey et al. (2006) were analyzed in the UW-Madison, Dept. of Geoscience Stable Isotope Laboratory by laser fluorination using $BrF_5$ as the reagent. A dual-inlet gas-source Finnigan/MAT 251 mass spectrometer was used to measure isotope ratios. Standardization was done using UWG-2 ($\delta^{18}O$ = 5.80 ‰ VSMOW), which provides high precision and accuracy in laser analyses (Valley et al. 1995). Values of $\delta^{18}O$ of whole rock powders (~2mg) of Dinkey Dome granite and Dinkey Creek sedimentary rocks were analyzed by laser fluorination using an airlock sample chamber (Spicuzza et al. 1998) (Supplementary Table E).

**SIMS analysis of $\delta^{18}O$ in zircon and garnet**

Oxygen isotope ratios were measured at the WiscSIMS Laboratory at UW-Madison with a CAMECA ims-1280 large-radius multicollector ion microprobe/SIMS (Kita et al. 2009; Valley and Kita 2009). Oxygen isotopes were analyzed using a 2.0–2.2 nA primary $Cs^+$ beam accelerated by 10 kV (impact energy = 20 kV) and focused on sample surface with ~10–12 μm spot diameter. Secondary $^{16}O$ and $^{18}O^-$ ions were measured by two Faraday cup detectors simultaneously. Zircon standard KIM-5 ($\delta^{18}O$ = 5.09 ‰ VSMOW; Valley 2003) and garnet standard UWG-2 ($\delta^{18}O$ = 5.80 ‰ VSMOW; Valley et al. 1995) were mounted in the center of each sample and used as running standards to bracket unknown sample analyses. Four consecutive measurements of the standard were made before and after every set of 10 sample analyses. Additional standardization and calibration of garnet standards was performed to account for the compositional effects on instrumental bias as described previously (Page et al. 2010, Russell et al. 2013, Kitajima et al. 2016). Typically, two analysis spots were made on each zircon (core and rim), and approximately 3-8 spots (rim to rim) on each garnet.

Cracks, inclusions, radiation-damaged zircon domains and other features that can compromise an analysis were avoided by secondary electron (SE), backscattered electron (BSE), and cathodoluminescence (CL) imaging of minerals before in situ analysis. In addition, all SIMS pits were imaged post-analysis using BSE and SE, and pits that hit cracks or contain mineral inclusions are culled from the final dataset (Supplementary Tables C-D).

**SIMS analysis of REEs in zircon**

Zircon grains were analyzed by SIMS for trace elements, including rare earth elements

(REEs) in the WiscSIMS Laboratory at UW-Madison with a CAMECA ims-1280. The following elements were analyzed: Li, Si, P, Ca, Ti, V, Fe, Y, La, Ce, Pr, Nd, Sm, Eu, Tb, Gd, Dy, Ho, Er, Tm, Yb, Lu, Hf, Th, and U (Supplementary Table F). Similar conditions as Page et al. (2007a) were used: impact energy of 23 kV, 4 nA $O^-$ ion beam shaped to a diameter of 25 μm on the sample surface and a secondary ion accelerating voltage of 10 kV. For trace element analysis, the configuration of the secondary ion optics was optimized for high transmission (Kita et al. 2009). A single electron multiplier, field aperture of 4000 μm, MRP of 3000, and secondary beam energy offset of 40 V were used and allow resolution of the selected REE peaks from the interfering REE oxides. Measured counts for each element were normalized to $^{30}Si$. During the analysis session, NIST-610 glass was used as a running standard. To estimate the matrix effects on relative sensitivity factor (RSF) between zircon and NIST 610, the zircon standards 91500 (Y, REE, Hf, Th and U: Wiedenbeck et al. 2004) and Xinjiang (Li: Ushikubo et al. 2008) were analyzed at the beginning of the trace element session. For Ti concentration, we used the correction factor on RSF between zircon and NIST-610 reported by Fu et al. (2008). No correction for matrix effect was applied on P, Ca, V and Fe because their concentrations in the 91500 zircon are unknown. Counting times were adjusted for NIST-610 because of the difference in REE composition in comparison to natural zircons (Page et al. 2007a) (Supplementary Table F).

## Petrography

The Dinkey Dome granite samples contain quartz, plagioclase, K-feldspar, zircon, biotite and muscovite, and commonly have garnet, perthite, sericitized feldspar, granophyre and myrmekite. Andalusite and sillimanite show scattered occurrence on the eastern side of the pluton (Guy 1980), and molybdenite and uraninite have been reported on the eastern side

(Lackey et al. 2006). Andalusite has textural traits indicative of magmatic crystallization, including uniformly sized and distributed, euhedral to subhedral grains free of carbonaceous chiastolite inclusions that are typically associated with metamorphic andalusite (Clarke et al. 2005). Where observed, fibrolitic sillimanite is uniformly distributed in the granite and does not appear to form at the expense of andalusite or vice versa. Analyses of $\delta^{18}O$ (And) in two samples showed values consistent with magmatic crystallization; values of 8.5‰ are ~2‰ lower than pluton $\delta^{18}O$ (WR) values whereas adjacent wallrock $\delta^{18}O$ values are 3-4‰ higher than andalusite and inconsistent with high temperature equilibrium. Values of $\delta^{18}O$ of fibrolite from one sample was similar to co-existing andalusite, a result consistent with crystallization of the two minerals from the same magma (Lackey et al. 2006). Overlap of muscovite-forming reactions and the $H_2O$-saturated solidus require higher pressures of crystallization than implied by magmatic andalusite or miarolitic cavities in the Dinkey Dome pluton. This observation suggests that muscovite in the Dinkey Dome granite is not a magmatic phase, implying varying P-T conditions. Alternatively, some $Al_2SiO_5$ (andalusite and/or sillimanite) phenocrysts may have formed during magma rising through the crust.

Unlike other peraluminous plutons in the Sierra Nevada where garnet is concentrated near contacts, magmatic garnet in the Dinkey Dome occurs throughout the entire pluton. The dominant metamorphic wall rocks in direct contact with the Dinkey Dome granite are biotite hornfels consisting of biotite, andalusite, cordierite, sillimanite, and quartz, and do not contain garnet.

**Zircon and Garnet: Occurrence, Morphology and Internal Structures**

Magmatic garnet occurs throughout the Dinkey Dome and is found in all the samples collected in this study and by Lackey et al. (2006). These garnets are generally subhedral to euhedral and range in size from 200-2000 μm. All samples contain pink and red garnets. Garnets in the west side of the pluton are darker (red) vs. lighter (pink) in the east side. BSE imaging reveals very subtle oscillatory zoning within these garnets. Garnets aren't generally inclusion-rich and the distribution of inclusions from garnet to garnet is not uniform throughout the samples. Garnets contain inclusions of plagioclase, K-feldspar, muscovite, biotite, quartz, monazite, apatite, ilmenite and zircon (Fig. 3).

Zircon in the Dinkey Dome granite occurs as euhedral crystals that range in size from 20 to 300 μm but are generally ~100 μm long and 25-50 μm wide. In some cases, zircon crystals occur as inclusions within garnet (Figs. 3c and d). Conversely, some zircons contain inclusions of quartz, K-feldspar, apatite, plagioclase, biotite, ilmenite, and magnetite that have been identified by EDS. Ortiz (2010) examined 50 zircons by SEM in a polished grain mount from sample 1S79 and found apatite inclusions in 9 zircon grains, K-feldspar in 8, quartz in 4, biotite in 2, and Fe-Ti oxide in 1. BSE and CL imaging were used to document the internal growth zoning in zircon. Dinkey Dome zircon mainly displays oscillatory zoning; convolute zoning is present in some cores. Representative textures are seen in Figure 4.

## Results

### Garnet Composition by EPMA

Garnet grains from the Dinkey Dome pluton are almandine-spessartine-rich with minor pyrope and grossular ($X_{Alm}$= 0.60-0.86; $X_{Sps}$ = 0.11-0.27; $X_{Pyp}$ = 0.01-0.07; $X_{Grs}$ = 0.02-0.06) (Fig. 5a). Most of the garnets analyzed in this study slightly increase in spessartine and decrease in almandine at the rims. Internal cation zoning is generally subtle, however crystals 1S52-02, 1S52-04, 1S80-04, and 10DD07b-02 show bell-shaped rim-to-rim profiles. Compositionally, garnet is similar to garnet from other Sierran granitoids (Guy and Wones 1980, Calk and Dodge

1986, Ague and Brimhall 1988a, Liggett 1990; Lackey et al. 2006). Values of $X_{Grs}$ are higher in western side of the pluton, suggesting slightly higher crystallization pressures. Crystals from the eastern side of the pluton have less pyrope and are generally more almandine-rich, which can explain the difference in color east to west (Fig. 5a).

**Oxygen isotope ratios by Laser Fluorination**

Laser fluorination analyses of oxygen isotope ratios in garnet from a west to east traverse (A-A’, Fig. 2 and 6) were conducted to assess variations between pink garnet (lower $X_{Alm}$) and red garnet. Only one of the samples analyzed (1S51) shows a variation in $\delta^{18}O$ between red (7.25 ±0.23‰ 2SD) and pink garnet (6.80 ±0.23‰); the other samples showing different color grains (1S77, 1S79, and 1S82) show no variation in $\delta^{18}O$.

Individual garnets from samples 1S51, 1S52, 1S53, 1S77, 1S79, 1S80, and 1S81 were handpicked and analyzed by both laser fluorination and SIMS (Supplementary Table E). Values of $\delta^{18}O$ obtained by laser fluorination for these grains average 6.90 ±0.18‰ (1SD) for the eastern side and 7.63 ±0.17‰ to the west. These values are similar to those obtained Lackey et al. (2006), who also reported lower $\delta^{18}O$ for garnet from the eastern part of the pluton.

Whole rock analyses where also made of granite and metasediment samples 10DD-02 through 10DD-22 (Table 1). The granite $\delta^{18}O$(WR) values range from 9.0 to 10.5‰, and the metasedimentary rocks (biotite hornfels and quartzite) range in $\delta^{18}O$(WR) from 11.7 to 12.8‰.

**Oxygen isotope ratios by SIMS**

**Garnet**

Garnets from the western side of the pluton analyzed by SIMS resemble the laser fluorination analysis (within uncertainty). In contrast, garnets from the eastern side of the pluton shows consistently lower values relative to laser fluorination analysis, with a difference of $\delta^{18}O$

values ranging from 0.6 to 1.5‰ (Fig. 6b) (Table 1). These differences likely result from quartz inclusions within garnet crystals that are higher in $\delta^{18}O$ and were unavoidably analyzed by laser fluorination. The SIMS analyses avoid inclusions that are plainly visible in polished surfaces and thus SIMS values of $\delta^{18}O$ are not affected by inclusions.

Values of $\delta^{18}O$ in epoxy-mounted garnet grains from western side of the pluton are higher (average $\delta^{18}O$(Grt) = 7.4 ±0.2‰) than eastern side $\delta^{18}O$(Grt) values of 6.3 ±0.2‰, and show no significant core to rim zoning in $\delta^{18}O$. Average values of $\delta^{18}O$ measured from garnets selected in thin section show a similar trend with higher values on the western side (6.9 ±0.3‰) and lower values on the eastern side (5.2 ±0.3‰). However, unlike garnet hand-picked from mineral separates, garnets in thin section show variation in $\delta^{18}O$ from rims to cores (Fig.7). The core to rim variation is more prominent on the larger (>1 mm) garnets from the northwestern side of the pluton. The zoning of the eastern-side garnets is more subtle and less common (Table 1).

This difference likely results due to analysis of larger subhedral garnets in thin section rather than the smaller equant garnets that were selected from mineral separates. It is also possible that the low $\delta^{18}O$ garnets are more delicate and were destroyed by the disk mill during sample processing. The $\delta^{18}O$ in garnets from thin sections on the east side is very low (ave. = 5.2 ±0.3‰). This pattern, combined with the observation of large miarolitic cavities in the east side of the pluton suggests the possibility of the garnet growing into the sub-solidus realms, with some non-magmatic water infiltrating the system. Studies of Cretaceous skarns in the south-central Sierra show that garnet growing in shallow hydrothermal systems may record multiple episodes of fluid flow and low-$\delta^{18}O$ domains record incursions of meteoric water at different times, including waning stages of garnet growth (e.g., D’Errico et al. 2012; Ryan-Davis et al.

2019). Therefore the Dinkey Dome garnets may be recording surface water infiltration on the East side.

**Zircon**

SIMS analyses of rims and cores of individual zircon grains from 10 Dinkey Dome samples along the A-A' traverse (Fig. 2, 1S51-1S82) show constant $\delta^{18}O$ values for the cores: 7.8 ±0.3‰ on the east side and 7.7 ±0.3‰ on the west side. The rims of the zircons have consistently lower $\delta^{18}O$ values that average 6.7 ±0.3‰ on the east side and 6.9 ±0.3‰ on the west side (Fig. 6a).

SIMS $\delta^{18}O$ values of zircon in thin sections from the eastern side average 7.2 ±0.2‰ (Fig. 6a, Table 1). The average $\delta^{18}O$ in each zircon from the western part of the pluton is 7.6 ±0.2‰. These values are consistent with SIMS data for zircon cores (7.7 to 7.8‰) that dominate the mass of each zircon. Zircons from some samples (10DD-02a-b, 10DD-05a, 10DD-16c, 10DD-17, and 10DD-19c) did not have rims that were distinguishable by CL.

**Trace elements in zircon**

Trace element compositions in cores and rims of grains from the Dinkey Dome granite are summarized in chondrite-normalized REE diagrams (Fig. 8). The REE data are consistent with igneous zircon from continental crust (Belousova et al. 1998; Hoskin and Ireland 2000; Belousova et al. 2002, Grimes et al. 2007) and show HREE enrichment, a positive Ce anomaly and a negative Eu anomaly (Fig. 8).

All zircon data plot within the 'magmatic' field in REE discriminant diagrams: $(Sm/La)_N$ vs. La (ppm) and Ce/Ce* $((Ce)_N/\sqrt{((La)_N(Pr)_N)}$ vs. $(Sm/La)_N$ (Figs. 9a and b). None of the cores or rims have REE compositions similar to hydrothermal zircon (Hoskin 2005). Although Chondrite normalized REE patterns are similar in cores and rims of grains (Fig. 8), $(Sm/La)_N$ vs.

La (ppm) and Ce/Ce* vs. $(Sm/La)_N$ are clearly bimodal, with rims having slightly flatter LREEs and being higher in [La] and lower $(Sm/La)_N$, (Figs. 9a and 9b).

## Discussion

The in situ measurements of $\delta^{18}O$ in garnet and zoned zircons reveal a more complex magmatic assimilation and fractional crystallization history for the Dinkey Dome granite than was resolved by bulk-mineral analysis. High- $\delta^{18}O$ zircon cores crystallized from an initially high- $\delta^{18}O$ magma derived by melting of a high-$\delta^{18}O$ source deeper in the crust (Figs. 10 and 11). The zircon cores average 7.7‰, indicating $\delta^{18}O$(magma) values of 9.4‰ [~69 wt. % $SiO_2$; $\Delta^{18}O(WR\text{-}Zrc) \approx 0.0612$ (wt.% $SiO_2$) – 2.5‰ (Lackey et al. 2008)]. The inclusions of zircon in garnet and the steep positive slope of HREEs in zircon indicate that the majority of garnet grew after zircon. Lower $\delta^{18}O$ values in the rims of zircon (ave. 6.8‰) and throughout most garnets show that a lower $\delta^{18}O$ contaminant, possibly hydrothermally altered rocks, was incorporated into the magmas at depth. The quartz and feldspars from the Dinkey Dome do not record such low $\delta^{18}O$ values (Lackey et al. 2006), however lack of zoning in these minerals may reflect resetting by late fluid exchange, thus not preserving a complete record of magmatic history. The assimilation and fractional crystallization history of the magma is preferentially preserved in zircon and garnet due to the minerals' slower diffusion rates relative to quartz and feldspar.

It is significant that no low $\delta^{18}O$ (< 5‰) rocks are identified in the pendant immediately adjacent to the Dinkey Dome pluton. Thus, the lower $\delta^{18}O$ domains in garnet and zircon point to this stage of melting and contamination of the magma at depths greater than final crystallization depths. The heterogeneous nature of the wallrock in the Sierran arc, which contains domains of Triassic and Jurassic hydrothermally altered volcanic wallrocks with relatively low $\delta^{18}O$ (e.g., Peck and Van Kooten 1983; D'Errico et al. 2012; Ryan-Davis et al. 2019). Such metavolcanic and metasedimentary wallrocks are the most likely source of a low- $\delta^{18}O$ assimilation signature. Evidence of melting is found where migmatite complexes are developed in metavolcanics rocks at mid- to lower-crustal level pendants in the southern Sierra Nevada (Saleeby et al. 2003). Nevertheless, thermal budgets of peraluminous magma prohibit significant melting and assimilation of wallrock at emplacement levels of the Dinkey Dome pluton, or mixing of magmas, thus the low- $\delta^{18}O$ assimilation may be restricted to a thin veneer of the eastern half of the pluton. Discrete zoning is shown by the heterogeneous nature of the Dinkey Dome pluton; the northwestern samples show a rim-ward shift to higher $\delta^{18}O$ in some garnet rims suggesting that as some of the magma was produced and transported, it encountered high- $\delta^{18}O$ rock and was locally contaminated (Fig. 11).

## Implications

In situ microanalysis of oxygen isotope ratios and trace elements from magmatic zircon and garnet in the Dinkey Dome pluton reveals a complex magmatic history. A clear lowering of $\delta^{18}O$ is recorded by both garnet and zircon, confirming that low- $\delta^{18}O$ melts, fluids, or both were incorporated into parts of the magma, at late stages. Given that the pluton was emplaced into its pendant rocks much earlier than many other plutons in the Shaver Intrusive suite, it would have been emplaced inboard of the active arc, and likely encountered a thicker, more heterogeneous crustal column and interactions with that crust superimposed additional contamination on the magma. The Dinkey Dome is not the only example in the region. The Grant Grove peraluminous granite, which shares similarities with Dinkey Dome, like being isolated by pendant rocks and surrounded by younger metaluminous plutons, shows higher $\delta^{18}O$ in its margins indicative of localized contamination (Lackey et al. 2006). That localized “veneer” of later contamination is manifested by additional growth of garnet and aluminosilicates at the margin of the pluton where it intruded and partially melted wallrock at emplacement levels. Later stage Sierran magmatism in the region was more voluminous, building larger plutons with more uniform compositions of magmas, a result of organization and homogenization of magma source regions (Lackey et al. 2012).

The Dinkey Dome pluton preserves an example of how early-stage plutons record crustal melting in nascent Cordilleran arcs. A comparable case is found in scattered peraluminous plutons that intrude the Julian Schist in the Peninsular Ranges batholith in southern California (Shaw et al. 2003). These Jurassic granites are relatively small compared the voluminous younger (Cretaceous) tonalite and granodiorite plutons that surround them, comprising most of the Peninsular Ranges batholith. Some of the Jurassic plutons are directly associated with migmatitic zones in the Julian Schist and have elevated $Sr_i$ (>0.71) and $\delta^{18}O$ (16-20‰), values that overlap with the schist itself indicating it was the source of the melts that produced the peraluminous plutons. Though of much greater age difference than the Dinkey Dome and younger plutons that surround it and associated pendant rocks, the progression from early, small peraluminous plutons to larger metaluminous plutons is the same. Unlike the Peninsular Ranges example, the Dinkey Dome does not have evidence of a localized migmatite complex, consistent with its shallow emplacement. In addition, the peraluminous plutons of the Peninsular Ranges contain abundant, Proterozoic zircon cores and crystals (Shaw et al. 2003), likely because melts from which they crystallized were saturated in zirconium and unable to dissolve grains inherited from their metasedimentary sources (e.g., Miller et al. 2003). The Dinkey Dome granite contains few inherited cores (Fig. 4). It follows is that the Dinkey Dome magmas were potentially derived from hotter or inheritance-poor sources (Miller et al. 2003) and presumably are farther separated from said source(s).

The findings from this study also raise the question of how, given their small size and thermal mass, high silica magmas can continue to actively interact with varied wallrocks and melts thereof at different depths in the arc. This is partially illustrated the Hall Mountain pluton in the Panamint Range, California (Mahood et al. 1996). Here, a roof zone with pegmatitic and aplitic domains is enriched in peraluminous minerals (garnet, muscovite) compared to lower in the pluton, however the entire pluton is peraluminous. The authors invoke in situ fractionation of the magma in the upper roof zone with additional melts also percolating up into the roof zone from the lower reaches of the pluton. In such a scenario, fractionationating melt increases peraluminosity (such as seen in the eastern Dinkey Dome pluton), and promotes additional growth of peraluminous minerals like garnet, sillimanite, and andalusite. Because fractionating peraluminous magmas sees increased concentrations of water and incompatible elements, this fractionation would counteract the tendency of cooling and crystallization to impede distribution of new melt into the "mushy" roof zone of the pluton (e.g., Scaillet et al. 2000). A similar process might have occurred in the eastern Dinkey Dome pluton whereby a more highly fractionated roof zone continued to receive melts and consequently achieved the isotopic heterogeneity seen in crystal-scale $\delta^{18}O$ zoning that was not recorded in the western domain. Sustained melt and fluid percolation in the east side also could have allowed low- $\delta^{18}O$ values to be recorded in some generations of garnet that continued to grow as peraluminosity increased. In contrast, the west side of the pluton crystallized relatively earlier and thus did not record incorporation of the low- $\delta^{18}O$ material and thus was more homogeneous in its composition.

Thus, the east and west sides of the Dinkey Dome pluton behaved as two magma batches, separated by a septum of metasediments, that accumulated, fractionated, and ultimately crystallized. The contrasting isotopic records preserved in individual garnets reveal how continental arc magmatism generates crustal melts that can be variably modified by later interactions with the crustal column. Given the isotopic heterogeneity in different sides of the pluton, and within crystals, we posit that crustal melts typically are produced in small volumes such as seen in magmatic complexes in the Sierra (Zeng et al. 2005) and Peninsular Ranges (Shaw et al. 2003). Thus, before an arc organizes a Melting-Assimilation-Storage-and Homogenization (MASH) system, hot zone (Annen et al. 2006), or similar magmatic source region capable of homogenizing unusual melt compositions, peraluminous plutonic "harbingers" like Dinkey Dome preserve of arc crustal structure. Moreover, such plutons provide subtle signals of shifts in greater tectono-magmatic systems; their distribution and character may record the onsets of magmatic "flare-up" events (e.g., DeCelles et al. 2009) and can potentially be used to identify cryptic crustal end members that become greatly diluted in larger granodiorite and tonalite magma systems during vigorous stages of arc magmatism.

## Acknowledgements

The authors thank Noriko Kita and the WiscSIMS group for assistance with SIMS analysis. We also thank John Fournelle for assistance with EPMA analysis, Mike Spicuzza for assistance with laser fluorination and Brian Hess who polished samples for this study. Adam Kinnard is thanked for assistance in field sampling. This study was supported by BP-UW Research Assistantship, the DOE 93ER14389 and NSF EAR-0838058 (JWV) and NSF EAR-0948706 (JSL). WiscSIMS is supported by National Science Foundation (EAR-1658823) and the University of Wisconsin – Madison.

## References

Ague, J.J., and Brimhall, G.H. (1988a) Magmatic arc asymmetry and distribution of anomalous plutonic belts in the batholiths of California: effects of assimilation, crustal thickness, and depth of crystallization. Geological Society of America Bulletin, 100, 912–927.

Ague, J.J., and Brimhall, G.H. (1988b) Regional variations in bulk chemistry, mineralogy, and the compositions of mafic and accessory minerals in the batholiths of California. Geological Society of America Bulletin, 100, 891–911.

Ardill, K., Paterson, S., and Memeti, V. (2018) Spatiotemporal magmatic focusing in upper-mid crustal plutons of the Sierra Nevada arc. Earth and Planetary Science Letters, 498, 88–100.

Annen, C., Blundy, J.D., and Sparks, R.S.J. (2006) The genesis of intermediate and silicic magmas in deep crustal hot zones: Journal of Petrology, 47, 505–539.

Bateman, P.C. (1992) Plutonism in the central part of the Sierra Nevada batholith, California. USGS Professional Paper, 1483, 186 p.

Bateman, P.C., and Wones, D.R. (1972) Geologic map of the Huntington lake quadrangle, central Sierra Nevada, California. USGS Geologic Quadrangle 987.

Belousova, E.A., Griffin, W.L., and Pearson, N.J. (1998) Trace element composition and cathodoluminescence properties of southern African kimberlitic zircons. Mineralogical Magazine, 62, 355–366.

Belousova, E.A., Griffin, W.L., O'Reilly, S.Y, and Fisher, N.I. (2002) Igneous zircon: trace element composition as an indicator of source rock type. Contributions to Mineralogy and Petrology, 143, 602–622.

Bindeman, I.N. (2008) Oxygen Isotopes in Mantle and Crustal Magmas as Revealed by Single Crystal Analysis. Reviews in Mineralogy and Geochemistry, 69, 445–478.

Bowman, J.R., Moser, D.E., Valley, J.W., Wooden, J.L., Kita, N.T., and Mazdab, F.K. (2011) Zircon U-Pb isotope, $\delta^{18}O$ and trace element response to 80 m.y. of high temperature formation. American Journal of Science, 311, 719–772.

Calk, L.C., and Dodge, F.C. (1986) Garnet in granitoid rocks of the Sierra Nevada Batholith, California. 14th International Mineralogical Association, Abstracts, p. 69.

Chapman, J.B., and Ducea, M.N. (2019) The role of arc migration in Cordilleran orogenic cyclicity. Geology, 47, 627–631.

Chappell, B.W., and White, A.J.R. (1974) Two contrasting granite types. Pacific Geology, 8, 173–174.

Chen J.H., and Moore J.G. (1982) Uranium-lead isotopic ages from the Sierra Nevada batholith, California. Journal of Geophysical Research, 87, 4761–4784.

Chin, E.J., Lee, C.T.A., and Barnes, J.D. (2014) Thickening, refertilization, and the deep lithosphere filter in continental arcs: Constraints from major and trace elements and oxygen isotopes. Earth and Planetary Science Letters, 397, 184-200.

Clarke, D.B., Dorais, M., Barbarin, B., Barker, D., Cesare, B., Clarke, G., El Baghdadi, M., Erdmann, S., Forster, H.J., Gaeta, M., and others (2005) Occurrence and Origin of Andalusite in Peraluminous Felsic Igneous Rocks. Journal of Petrology 46, 441–472.

Clemens, J.D., and Wall, V.J. (1981) Origin and crystallization of some peraluminous (S-type) granitic magmas. Canadian Mineralogist, 19, 111–131.

Coleman, D.S., and Glazner, A.F. (1997) The Sierra Crest magmatic event: rapid formation of juvenile crust during the late Cretaceous in California. International Geological Review, 39, 768–787.

Coleman, D.S., Gray, W., Glazner, A.F. (2004) Rethinking the emplacement and evolution of zoned plutons: Geochronologic evidence for incremental assembly of the Tuolumne Intrusive Suite, California. Geology, 32, 433–436.

Coughlan, R.A. (1990) Studies in diffusional transport: grain boundary transport of O in feldspars, diffusion of O, strontium, and the REEs in garnet and thermal histories of granitic intrusions in south-central Maine using O isotopes, 476 p. Ph.D. thesis, Brown University, Providence.

Davis, J.W., Coleman, D.S., Gracely, J.T., Gaschnig, R., and Stearns, M. (2012) Magma accumulation rates and thermal histories of plutons of the Sierra Nevada batholith, CA. Contributions to Mineralogy and Petrology, 163, 449–465.

DeCelles, P.G., Ducea, M.N., Kapp, P., and Zandt, G. (2009) Cyclicity in Cordilleran orogenic systems. Nature Geoscience, 2, 251-257.

D'Errico, M.E., Lackey, J.S., Surpless, B.E., Loewy, S.L., Wooden, J.L., Barnes, J.D., Strickland, A., and Valley, J.W. (2012) A detailed record of shallow hydrothermal fluid flow in the Sierra Nevada magmatic arc from low-$\delta^{18}$O skarn garnets. Geology, 40, 763–766.

Dorais, M.J., Whitney, J.A., and Roden, M.F. (1990) Origin of Mafic Enclaves in the Dinkey Creek Pluton, Central Sierra Nevada Batholith, California. Journal of Petrology, 31, 853–881.

Ducea, M.N. (2001) The California arc: Thick granitic batholiths, eclogitic residues, lithospheric-scale thrusting and magmatic flare-ups. Geological Society of America Today, 11, 4–10.

Finch, J.R., Hanchar, J.M., Hoskin, P.W.O., and Burns, P.C. (2001) Rare-earth elements in synthetic zircon: Part 2. A single-crystal X-ray study of xenotime substitution. American Mineralogy, 86, 681–689.

Fliedner, M.M., Klemperer, S.L., and Christensen, N.I. (2000) Three-dimensional seismic model of the Sierra Nevada arc, California, and its implications for crustal and upper mantle composition. Journal of Geophysical Research, 105, 10899–10921.

Frazer, R.E., Lackey, J.S., and Valencia, V.A. (2008) New U-Pb zircon ages of the granites of the Dinkey Dome; reexamining the origins of the Shaver Intrusive Suite. Geological Society of America, Abstracts with programs, 41, pp 14.

Frost, B.R., Barnes, C.G., Collins, W.J., Arculus, R.J., Ellis, D.J., and Frost, C.D. (2001) A geochemical classification for granitic rocks. Journal of Petrology, 42, 2033–2048.

Fu, B., Page, F.Z., Cavosie, A.J., Fournelle, J., Kita, N.T., Lackey, J.S., Wilde, S.A., and Valley, J.W. (2008) Ti-in-zircon thermometry: applications and limitations. Contributions to Mineralogy and Petrology, 156, 197-215.

Grimes, C.A., John, B.E., Kelemen, P.B., Mazdab, F.K., Wooden, J.L., Cheadle, M.J., Hanghøj, K., and Schwartz, J.J. (2007) Trace element chemistry of zircons from oceanic crust: A method for distinguishing detrital zircon provenance. Geology, 35, 643–646.

Guy, R.E. (1980) The Dinkey Creek intrusive series, Huntington Lake Quadrangle, Fresno County, California, 125 p., MS thesis, Virginia Polytechnic Institute, Blacksburg.

Guy, R.E., and Wones, D.R. (1980) Petrology of the Dinkey Creek Intrusive Series, Huntington Lake Quadrangle, Fresno County, California. Geological Society of America, Abstracts with programs, 12, pp 440.

Halden, N.M., Hawthorne, F.C., Campbell, J.L., Teesdale, W.J., Maxwell, J.A., and Higuchi, D. (1993) Chemical characterization of oscillatory zoning and overgrowths in zircon using 3 MeV μ-PIXE. Canadian Mineralogist, 31, 637–647.

Halliday, A.N., Stephens, W.E., and Harmon, R.S. (1981) Isotopic and chemical constraints on the development of peraluminous Caledonian and Acadian granites. Canadian Mineralogist, 19, 205–216.

Hinton, R.W., and Upton, B.G.J. (1991) The chemistry of zircon: variations within and between large crystals from syenite and alkali basalt xenoliths. Geochimica et Cosmochimica Acta, 55, 3287–3302.

Hoskin, P.W.O. (2005) Trace-element composition of hydrothermal zircon and the alteration of Hadean zircon from the Jack Hills, Australia. Geochimica et Cosmochimica Acta, 69, 637–648.

Hoskin, P.W.O., and Ireland, T.R. (2000) Rare earth element chemistry of zircon and its use as a provenance indicator. Geology, 28, 627 – 630.

Hoskin, P.W.O., and Schaltegger, U. (2003) The composition of zircon and igneous metamorphic petrogenesis. Reviews in Mineralogy and Geochemistry, 53, 27–62.

Hoskin, P.W.O., Kinny, P.D., Wyborn, D., and Chappell, B.W. (2000) Identifying accessory mineral saturation during differentiation in granitoid magmas: an integrated approach. Journal of Petrology, 41, 1365–1396.

Jeon, H., Williams, I.S., and Chappell, B.W. (2012) Magma to mud to magma: rapid crustal recycling by Permian granite magmatism near the eastern Gondwana margin. Earth and Planetary Science Letters, 319-320, 104–117.

Kelly, J.L., Fu, B., Kita, N.T., and Valley, J.W. (2007) Optically continuous silcrete quartz cements of the St. Peter Sandstone: High precision oxygen isotope analysis by ion microprobe. Geochimica et Cosmochimica Acta, 71, 3812 – 3832.

King, E.M., and Valley, J.W. (2001) The source, magmatic contamination, and alteration of the Idaho batholith. Contributions to Mineralogy and Petrology, 142, 72–88.

Kistler, R.W. (1990) Two different lithosphere types in the Sierra Nevada, California. In: J.L. Anderson, Eds., The nature and origin of Cordilleran magmatism, Geological Society of America Memoir, 174, 271–281, Geological Society of America, Boulder.

Kistler, R.W., and Peterman, Z.E. (1973) Variations in Sr, Rb, K, Na, and Initial Sr87/Sr86 in Mesozoic Granitic Rocks and Intruded Wall Rocks in Central California. Geological Society of America Bulletin, 84, 3489–3512.

Kita, N.T., Ushikubo, T., Fu, B., and Valley, J.W. (2009) High Precision SIMS Oxygen Isotope Analyses and the Effect of Sample Topography. Chemical Geology, 264, 43–57.

Kitajima, K., Strickland, A., Spicuzza, M.J., Tenner, T.J., and Valley, J.W. (2016) Improved matrix correction of $\delta^{18}O$ analysis by SIMS for pyralspite and Cr-pyrope garnets. Goldschmidt Conference, 1542, Yokohama, Japan.

Lackey, J.S., Valley, J.W., and Hinke, H.J. (2006) Deciphering the source and contamination history of peraluminous magmas using $\delta^{18}O$ of accessory minerals: examples from garnet-bearing plutons of the Sierra Nevada Batholith. Contributions to Mineralogy and Petrology, 151, 20–44.

Lackey, J.S., Valley, J.W., Chen, J.H., and Stockli, D.F. (2008) Dynamic Magma Systems, Crustal Recycling, and Alteration in the Central Sierra Nevada Batholith: The Oxygen Isotope Record. Journal of Petrology. 49, 1397–1426.

Lackey, J.S., Erdmann, S., Hark, J.S., Nowak, R.M., Murray, K.E., Clarke, D.B., and Valley, J.W. (2011) Tracing garnet origins in granitoid rocks by oxygen isotope analysis: Examples from the South Mountain Batholith, Nova Scotia. Canadian Mineralogist, 49, 417–439.

Lackey, J.S., Cecil, M.R., Windham, C.J., Frazer, R.E., Bindeman I.N., and Gehrels, G. (2012) The Fine Gold Intrusive Suite: The Roles of Basement Terranes and Magma Source Development in the Early Cretaceous Sierra Nevada Batholith. Geosphere, 8, 292–313.

Lee, C.T., Cheng, X., and Horodyskyj, U. (2006) The development and refinement of continental arcs by primary basaltic magmatism, garnet pyroxenite accumulation, basaltic recharge and delamination: insights from the Sierra Nevada, California. Contributions to Mineralogy and Petrology, 151, 222 - 242.

Liggett, D.L. (1990) Geochemistry of the garnet bearing Tharps Peak Granodiorite and its relation to other members of the Lake Kaweah Intrusive Suite, southwestern Sierra Nevada, California In: J.L. Anderson, Eds., The nature and origin of Cordilleran magmatism, pp. 205-236. Geological Society of America Memoir, 174, Geological Society of America.

Mahood, G.A., Nibler, G.E., and Halliday, A.N. (1996) Zoning patterns and petrologic processes in peraluminous magma chambers: Hall Canyon pluton, Panamint Mountains, California. Geological Society of America Bulletin, 108, 437–453.

Memeti, V., Paterson, S., Matzel, J., Mundil, R., and Okaya, D. (2010) Magmatic lobes as “snapshots” of magma chamber growth and evolution in large, composite batholiths: an example from the Tuolumne Intrusion, Sierra Nevada, CA, Geological Society of America Bulletin, 122, 1912–1931.

Miller, C.F., McDowell, S.M., and Mapes, R.W. (2003) Hot and cold granites? Implications of zircon saturation temperatures and preservation of inheritance. Geology, 31, 529–532.

Moore, J.G., and Dodge, F.C.W. (1980) Late Cenozoic volcanic rocks of the southern Sierra Nevada, California: Part I. Geology and Petrology summary. Geological Society of America Bulletin, 91, 515–518.

O'Neil, J.R. and Chappell, B.W. (1977) Oxygen and hydrogen isotope relation in the Berridale batholith. Journal of the Geological Society, 133, 559–571.

Ortiz, D.M. (2010) Mineral inclusions in zircons: A tool for provenance analysis of sedimentary rocks, MS thesis, pp.44. University of Wisconsin, Madison.

Page, F.Z., Fu, B., Kita, N.T., Fournelle, J., Spicuzza, M.J., Schulze, D.J., Viljoen, F., Basei, M.A.S., and Valley, J.W. (2007a) Zircons from kimberlite: new insights from oxygen isotopes, trace element, and Ti in zircon thermometry. Geochimica et Cosmochimica Acta 71, 3887–3903.

Page, F.Z., Ushikubo, T., Kita, N.T., Riciputi, L.R., and Valley, J.W. (2007b) High precision oxygen isotope analysis of picogram samples reveals 2-µm gradients and slow diffusion in zircon. American Mineralogist, 92, 1772–1775.

Page, F.Z., Kita, N.T., *and* Valley, J.W. (2010) Ion microprobe analysis of oxygen isotopes in garnets of complex chemistry. Chemical Geology, 270, 9–19.

Patiño Douce, A.E., and Johnston, A.D. (1991) Phase equilibria and melt productivity in the pelitic system: implications for the origin of peraluminous granitoids and aluminous granulites. Contributions to Mineralogy and Petrology, 107, 202–218.

Peck, D.L., and Van Kooten, G. (1983) Merced Peak Quadrangle, Central Sierra Nevada, California-Analytic Data. US Geological Survey Professional Paper 1170-D, 29 p.

Ratajeski, K., Sisson, T.W. & Glazner, A.F. (2005) Experimental and geochemical evidence for derivation of the El Capitan Granite, California, by partial melting of hydrous gabbroic lower crust. Contributions to Mineralogy and Petrology, 149, 713–734.

Russell, A.K., Kitajima, K., Strickland, A., Medaris Jr., L.G., Schulze, D.J., and Valley, J.W. (2013) Eclogite-facies Fluid Infiltration: Constraints from $\delta^{18}O$ Zoning in Garnet. Contributions to Mineralogy and Petrology, 165, 103–116.

Ryan-Davis, J., Lackey, J.S., Gevedon, M., Barnes, J.D., Lee, C.T., Kitajima, K., and Valley, J.W. (2019) Andradite skarn garnet records of exceptionally low $\delta^{18}O$ values within an Early Cretaceous hydrothermal system, Sierra Nevada, CA. Contributions to Mineralogy and Petrology, 174, 68, 1–19.

Saleeby, J., Ducea, M., and Clemens Knott, D. (2003) Production and loss of high-density batholithic root, southern Sierra Nevada, California. Tectonics, 22.

Sawka, W.N., and Chappell, B.W. (1988) Fractionation of uranium, thorium and rare earth elements in a vertically zoned granodiorite: Implications for heat production distributions in the Sierra Nevada batholith. Geochimica et Cosmochimica Acta, 52, 1131–1143.

Scaillet, B., Whittington, A., Martel, C., Pichavant, H., and Holtz, F. (2000) Phase equilibrium constraints on the viscosity of silicic magmas II: implications for mafic-silicic mixing processes. Transactions of the Royal Society of Edinburgh-Earth Sciences, 91, 61-72.

Scaillet, B., Holtz, F., and Pichavant, M. (2016) Experimental Constraints on the Formation of Silicic Magmas. Elements, 12, 109-114.

Sisson, T.W., Ratajeski, K., Hankins, W.B. et al. (2005) Voluminous granitic magmas from common basaltic sources. Contributions to Mineralogy and Petrology, 148, 635–661

Shaw, S.E., Todd, V.R., and Grove, M. (2003) Jurassic peraluminous gneissic granites in the axial zone of the Peninsular Ranges, Southern California, in S. E. Johnson, S. R. Paterson, J. M. Fletcher, G. H. Girty, D. L Kimbrough., and B. A. Martin, Eds., Tectonic evolution of northwestern Mexico and the Southwestern USA, pp. 157–183, Geological Society of America Special Paper, Boulder, Colorado.

Speer, J.A. (1982) Zircon. Reviews in Mineralogy, 5, 67–112.

Spicuzza, M.J., Valley, J.W., and McConnell, V.S. (1998) Oxygen isotope analysis of whole rock via laser fluorination: an air-lock approach. Geological Society of America, Abstracts with programs, 30, pp. 80.

Taylor, H.P. and Sheppard, S.M.F. (1986) Igneous Rocks: 1. Processes of Isotopic Fractionation and Isotope Systematics. Reviews in Mineralogy and Petrology, 16, 227–272.

Tobisch, O.T., Renne, P.R., and Saleeby, J.B. (1993) Deformation resulting from regional extension during pluton ascent and emplacement, central Sierra Nevada, California. Journal of Structural Geology, 15, 609–628.

Tobisch, O.T., Fiske, R.S., Saleeby, J.B., Holt, E., and Sorensen, S.S. (2000) Steep tilting of metavolcanic rocks by multiple mechanisms, central Sierra Nevada, California. Geological Society of America Bulletin, 112, 1043-1058.

Ushikubo, T., Kita, N.T., Cavosie, A.J., Wilde, S.A., Rudnick, R.L., and Valley, J.W. (2008) Lithium in Jack Hills zircons: Evidence for extensive weathering of Earth's earliest crust. Earth and Planetary Science Letters, 272, 666–676.

Valley, J.W. (2003) Oxygen isotopes in zircon. Reviews in Mineralogy and Geochemistry, 53, 343–385.

Valley, J.W., and Kita, N.T. (2009) In situ Oxygen Isotope Geochemistry by Ion Microprobe. In M. Fayek M., Eds., MAC Short Course: Secondary Ion Mass Spectrometry in the Earth Sciences, 41, 19–63.

Valley, J.W., Kitchen, N.E., Kohn, M.J., Niendorf, C.R., and Spicuzza, M.J. (1995) UWG-2, A garnet standard for oxygen isotope ratio: strategies for high precision and accuracy with laser heating. Geochimica et Cosmochim Acta, 59, 5223–5231.

Valley, J.W., Lackey, J.S., Cavosie, A.J., Clechenko C.C., Spicuzza M.J., Basei M. A. S., Bindeman, I., Ferreira V., Sial A. N., King E. M., Peck W. H., Sinha A. K., and Wei C. S. (2005) Contributions to Mineralogy and Petrology, 150, 561–580.

Vielzeuf, D., Veschambre, M., and Brunet, F. (2005) Oxygen isotope heterogeneities and diffusional profiles in composite metamorphic/magmatic garnets from the Pyrenees. American Mineralogist, 90, 462–472.

Villaros, A., Stevens, G., Moyen, J.F., and Buick, I.S. (2009) The trace element compositions of S-type granites: evidence for disequilibrium melting and accessory phase entrainment in the source. Contributions to Mineralogy and Petrology, 158, 543–561.

Watson, E.B., and Cherniak, D.J. (1997) Oxygen diffusion in zircon. Earth and Planetary Science Letter, 148, 527–544.

Wenner J.M, and Coleman, D.S. (2004) Magma mixing and Cretaceous crustal growth: geology and geochemistry of granites in the central Sierra Nevada Batholith, California. International Geology Review, 46, 880-903.

Wiedenbeck, M., Hanchar, J.M., Peck, W.H., Sylvester, P., Valley, J.W., Whitehouse, M., Kronz A., Morishita, Y., Nasdala, L., Fiebig, J., and others (2004) Further Characterisation of the 91500 Zircon Crystal. Geostandards and Geoanalytical Research, 28, 9–39.

Wones, D.R., Hon, R., and Bateman, P.C. (1969) Depth of crystallization of a garnet-bearing quartz monzonite of the Sierra Nevada Batholith. Eos Transactions, American Geophysical Union, 50, 329.

Wright, K., Freer, R., Catlow, C.R.A. (1995) Oxygen diffusion in grossular and some geological implications. American Mineralogist, 80, 1020–1025.

Zen, E. (1988) Phase relations of peraluminous granitic rocks and their petrogenetic implications. Annual Reviews in Earth and Planetary Science, 16, 21–51.

Zeng, L., Ducea, M., and Saleeby, J.B. (2005) Geochemical characteristics of crustal anatexis during the formation of migmatite at the southern Sierra Nevada, California. Contributions to Mineralogy and Petrology, 150, 386–402.

## List of figure captions

Figure 1. Generalized map of the Central Sierra Nevada region, showing the location of peraluminous plutons and the study area, Dinkey Dome granite. Initial $^{87}Sr/^{86}Sr$=0.706 and PA/NA= Panthalassan/North American Break from Kistler (1990). The high $\delta^{18}O$(Zrn) (6.5-7.5‰) and low $\delta^{18}O$(Zrn) (5.5-6.5‰) domains of the central Sierra Nevada intrusives are modified from Lackey et al. (2006, 2008).

Figure 2. Geologic map of the Dinkey Dome with sample sites from this study and Lackey et al. (2006). Map after Bateman and Wones (1972).

Figure 3. Garnet and associated minerals in the Dinkey Dome granite. Sample 10DD02a. Images a and b were taken under transmitted light (PPL= Plain polarized light, XPL= Cross polarized light). Image c is a backscattered electron image (BSE) and shows quartz, muscovite, apatite, ilmenite and zircon, included in a typical garnet from the Dinkey Dome pluton.

Figure 4. Cathodoluminescence (CL) images of zircon grains from grain mounts 1S51-1S82 (Transect A-A' Fig. 2). Circles represent SIMS spots and numbers represent oxygen isotope ratios ($\delta^{18}O$). SIMS spots are 10 μm; scale bars are 50μm.

Figure 5. Cation composition of garnet phenocrysts from grain mounts and thin sections. (a) Almandine–spessartine–pyrope ternary plot includes garnet from both sides of the Dinkey Dome, showing that east side garnet is closer to the almandine-spessartine binary than garnet from the western half. (b) Representative rim-to-rim zoning profiles through the cores of garnets from samples 10DD06b-05 (west) and 10DD19c-02 (east). Background information for data presented in this figure can be found in supplementary data table B.

Figure 6. Oxygen isotope ratios in zircon (a) and garnet (b), and $\Delta^{18}O$ ($Grt_{Ave}$-$Zrc_{Ave}$) from a traverse of the Dinkey Dome pluton (A-A' in Fig. 2) measured by ion microprobe (this study) and laser fluorination data of Lackey et al. (2006). Data represents zircon and garnet from grain mounts (1S51-1S82) and thin sections (10DD-02-10DD-19). Samples on x-axis are spaced according to relative distance of their field localities. See figure 2 for sample localities. Background information for data presented in this figure can be found in supplementary data tables A, C-D.

Figure 7. Example of a rim-rim traverse of oxygen analyses for a single garnet (10DD-02a-13) in thin section, measured by SIMS, red symbols represent cores, and blue symbols are rim analyses.

Figure 8. Chondrite normalized REE patterns for zircons from four samples measured by SIMS (a. 1S82, b. 1S53, c. 1S79, d. 1S77) from the Dinkey Dome (1S82 and 1S79 from the west side, 1S53 and 1S77 from the east side). Filled symbols are from cores and open symbols are rims.

Background information for data presented in this figure can be found in supplementary data table F.

Figure 9. (a) $(Sm/La)_N$ vs. La (ppm) in rims and cores of zircon in the Dinkey Dome, from the same four samples from figure 8 (1S82, 1S53, 1S79, 1S77). (b) Ce/Ce* vs. $(Sm/La)_N$ in rims and cores from zircon in the Dinkey Dome, from the same four samples as in (a) (1S82, 1S53, 1S79, 1S77). Magmatic and hydrothermal fields from Hoskin (2005) and Grimes et al. (2007). Background information for data presented in this figure can be found in supplementary data table E.

Figure 10. Evolution of $\delta^{18}O$ in the Dinkey Dome pluton recording assimilation and fractional crystallization through time for the (a) western and (b) eastern sides of the pluton.

Figure 11. Model of the genesis of the Dinkey Dome pluton from the earliest stage (I) increments of melt transiting wallrocks of different $\delta^{18}O$ in the presence of early stage zircon, to (IV) final stage crystallization of garnet in the composite pluton.

Table 1. Oxygen isotope data summary.

| Sample | Lithology | $\delta^{18}O$ WR ‰ VSMOW (laser) | $\delta^{18}O$ Zrn ‰ VSMOW (laser) | $\delta^{18}O$ Zrn ‰ VSMOW (SIMS) | $\delta^{18}O$ Grt ‰ VSMOW (laser) | $\delta^{18}O$ $Grt_{Ave}$ ‰ VSMOW (SIMS) | $\Delta^{18}O$ ($Grt_{Ave}$-$Zrc_{Ave}$) ‰ VSMOW (SIMS) |
|---|---|---|---|---|---|---|---|
| 1S51 | granite | 9.71* | 7.76* | C=7.6, R=7.3 | 6.9 | 6.2 | -1.4 |
| 1S52 | granite | 9.80* | 7.51* | C=7.8, R=6.7 | 7.4 | 5.9 | -1.3 |
| 1S53 | granite | 9.57* | 7.53* | C=7.9, R=6.4 | 6.9 | 5.9 | -1.4 |
| 1S54 | granite | 9.90* | 7.81* | C=8.0, R=6.8 | | 6.4 | -1.0 |
| 1S58 | granite | 9.90* | 7.77* | C=7.5, R=7.0 | | 7.4 | 0.1 |
| 1S77 | granite | 9.81* | 7.63* | C=7.6, R=6.5 | 6.9 | 7.0 | -0.4 |
| 1S79 | granite | 9.96* | 7.67* | C=7.6, R=6.8 | 7.7 | 7.5 | 0.2 |
| 1S80 | granite | 10.30* | 7.72* | C=8.1, R=6.3 | 7.9 | 7.3 | 0.1 |
| 1S81 | granite | 9.79* | 7.76* | C=7.7, R=7.1 | 7.2 | 7.4 | 0.0 |
| 1S82 | granite | 9.79* | 7.73* | C=7.8, R=7.3 | 8.0 | 7.6 | -0.1 |
| 10DD-02 | granite | 10.47 | | 7.9** | | 7.1 | -0.8 |
| 10DD-05 | granite | 10.14 | | 7.4** | | 6.7 | -0.7 |
| 10DD-06 | granite | 9.65 | | | | | |
| 10DD-07 | granite | 9.41 | | | | | |
| 10DD-08 | granite | 9.48 | | | | | |
| 10DD-10 | bt hornfel | 12.72 | | | | | |
| 10DD-15 | quartzite | 11.82 | | | | | |
| 10DD-16 | granite | 9.35 | | 7.6** | | 5.7 | -1.9 |
| 10DD-17 | granite | 9.12 | | 6.9** | | 5.1 | -2.0 |
| 10DD-18 | granite | 8.96 | | | | | |
| 10DD-19 | granite | 9.06 | | 7.0** | | 5.0 | -2.0 |
| 10DD-20 | enclave | 8.25 | | | | | |
| 10DD-21 | granite | 9.17 | | | | | |
| 10DD-22 | granite | 9.06 | | | | | |

*Lackey et al. (2006) oxygen isotope analyses by Laser Fluorination.
**SIMS analyses on grains too small to distinguish core vs. rim.
C=Core, R=Rim; Zrn=Zircon, Grt=Garnet, WR=Whole Rock.
Samples 1S51 - 1S82 are grain mounts; 10DD-02 - 10DD-22 are thin sections.

**Supplementary Data Tables:**

Supplementary Table A: Sample locations and $\delta^{18}O$ summary.

Supplementary Table B: EPMA data.

Supplementary Table C: Zircon SIMS $\delta^{18}O$ data.

Supplementary Table D: Garnet SIMS $\delta^{18}O$ data.

Supplementary Table E: Garnet Laser Fluorination $\delta^{18}O$ data.

Supplementary Table F: Zircon REE data.

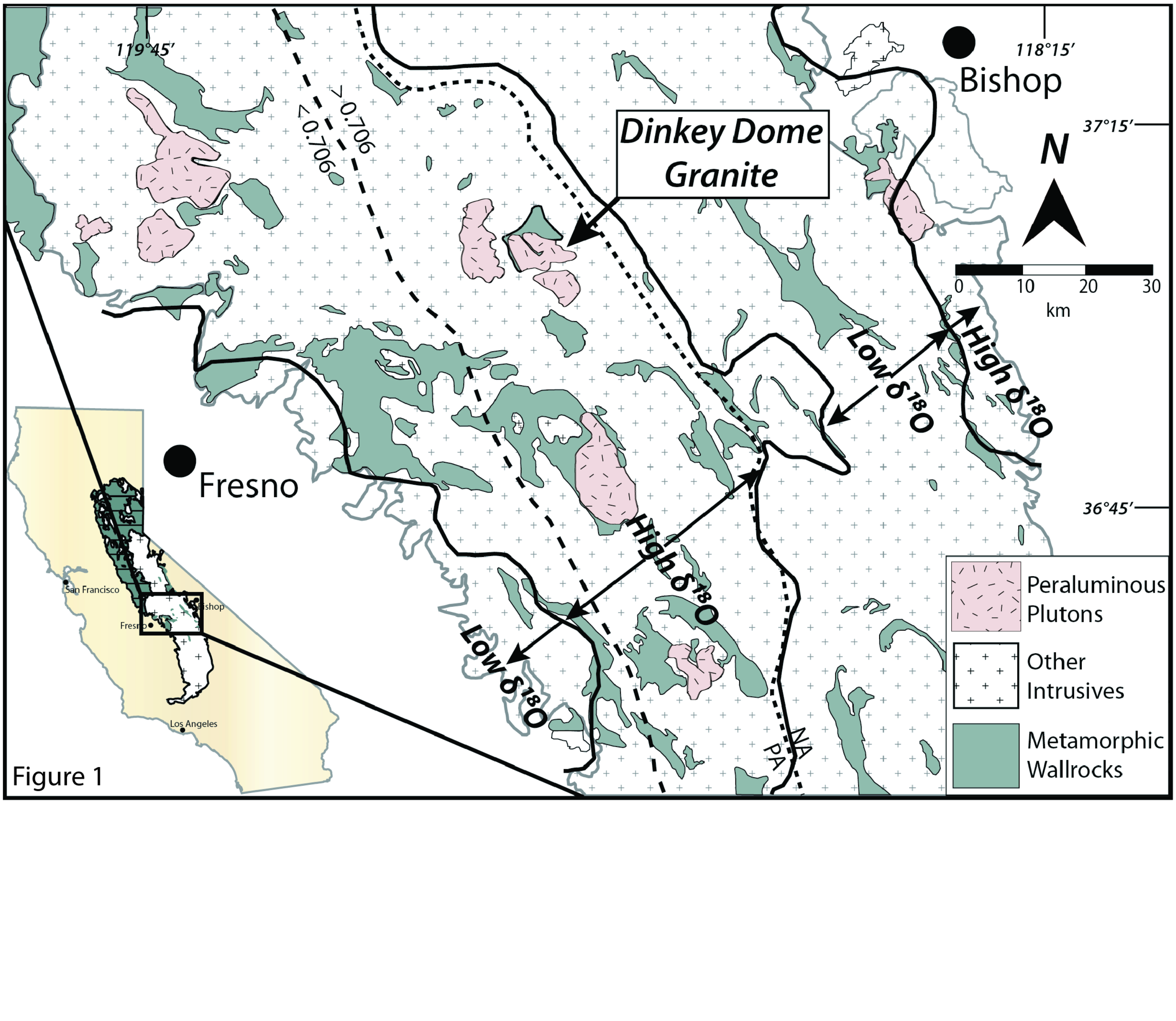
119°45′
118°15′
37°15′
36°45′
Bishop
Fresno
Dinkey Dome Granite
N
0 10 20 30
km
> 0.706
< 0.706
High δ18O
Low δ18O
NA
PA
Peraluminous Plutons
Other Intrusives
Metamorphic Wallrocks
San Francisco
Los Angeles

Figure 1

Figure 2

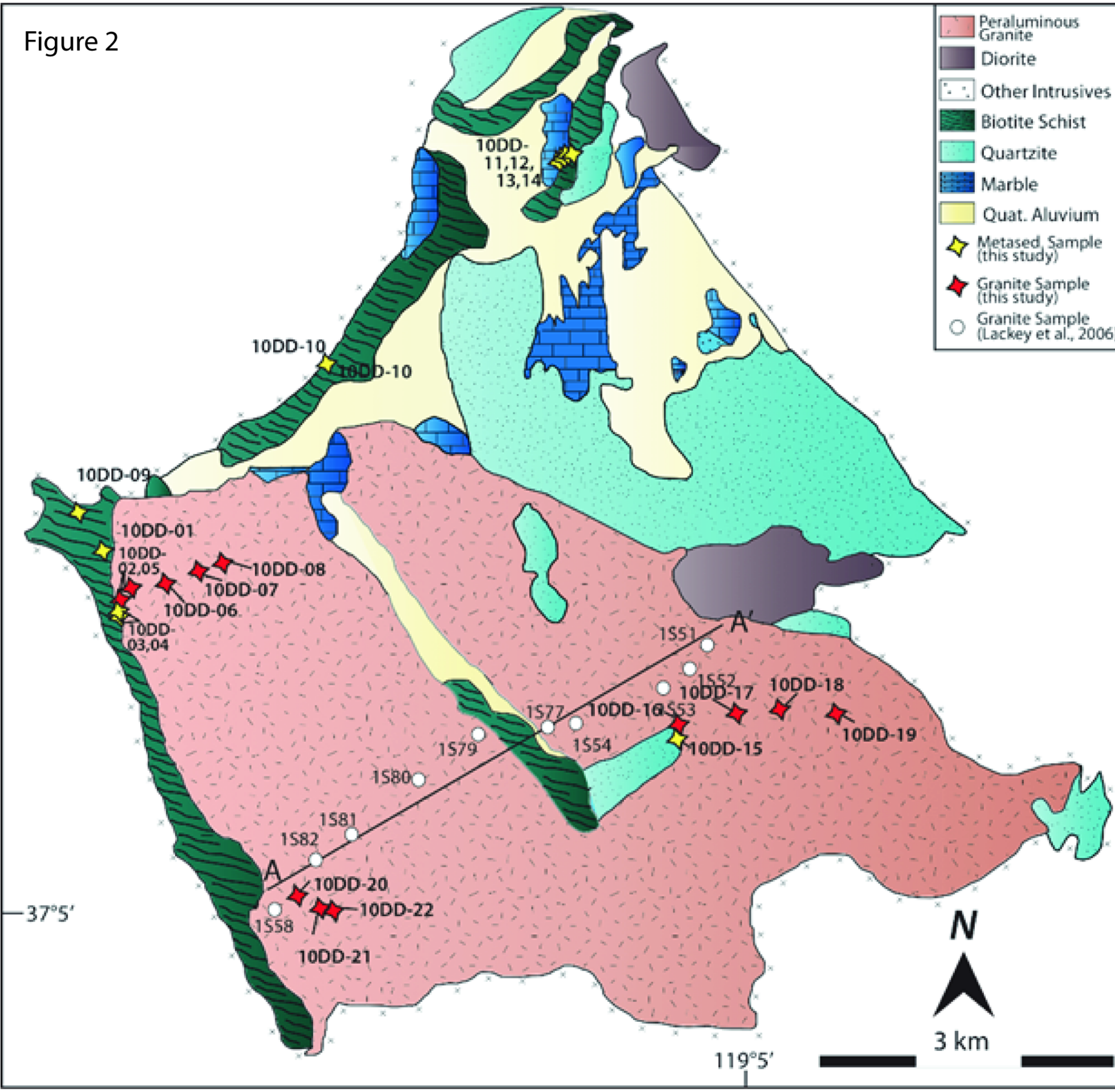

Peraluminous Granite
Diorite
Other Intrusives
Biotite Schist
Quartzite
Marble
Quat. Aluvium
Metased. Sample (this study)
Granite Sample (this study)
Granite Sample (Lackey et al., 2006)
10DD-11,12,13,14
10DD-10
10DD-10
10DD-09
10DD-01
10DD-02,05
10DD-08
10DD-07
10DD-06
10DD-03,04
A'
1S51
1S52
10DD-17
10DD-18
1S77
10DD-16
1S53
1S54
10DD-19
10DD-15
1S79
1S80
1S81
1S82
A
10DD-20
10DD-22
1S58
10DD-21
37°5′
119°5′
N
3 km

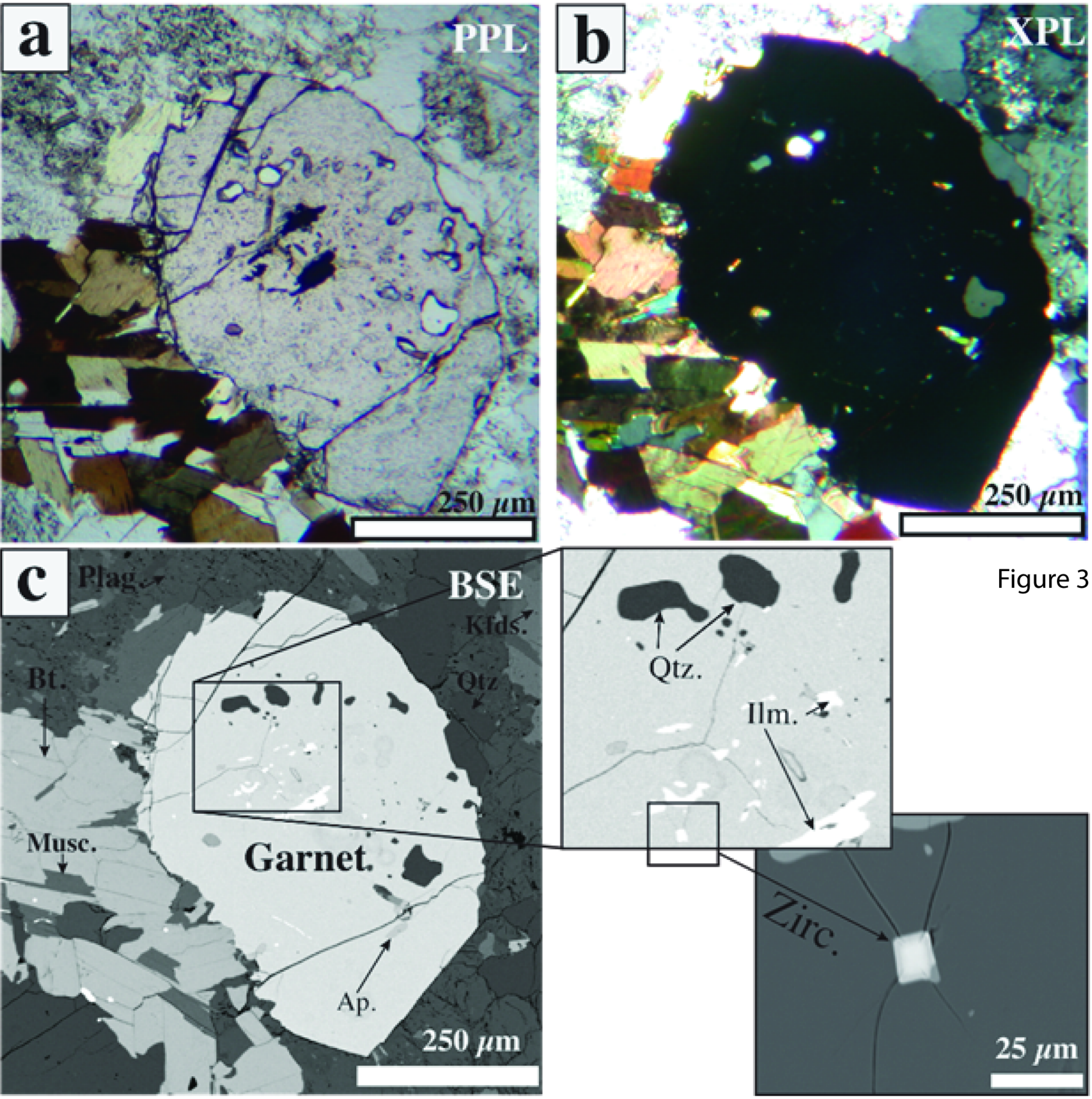
a
PPL
250 μm
b
XPL
250 μm
c
BSE
Plag.
Kfds.
Bt.
Qtz
Musc.
Garnet
Ap.
250 μm
Qtz.
Ilm.
Zirc.
25 μm

Figure 3

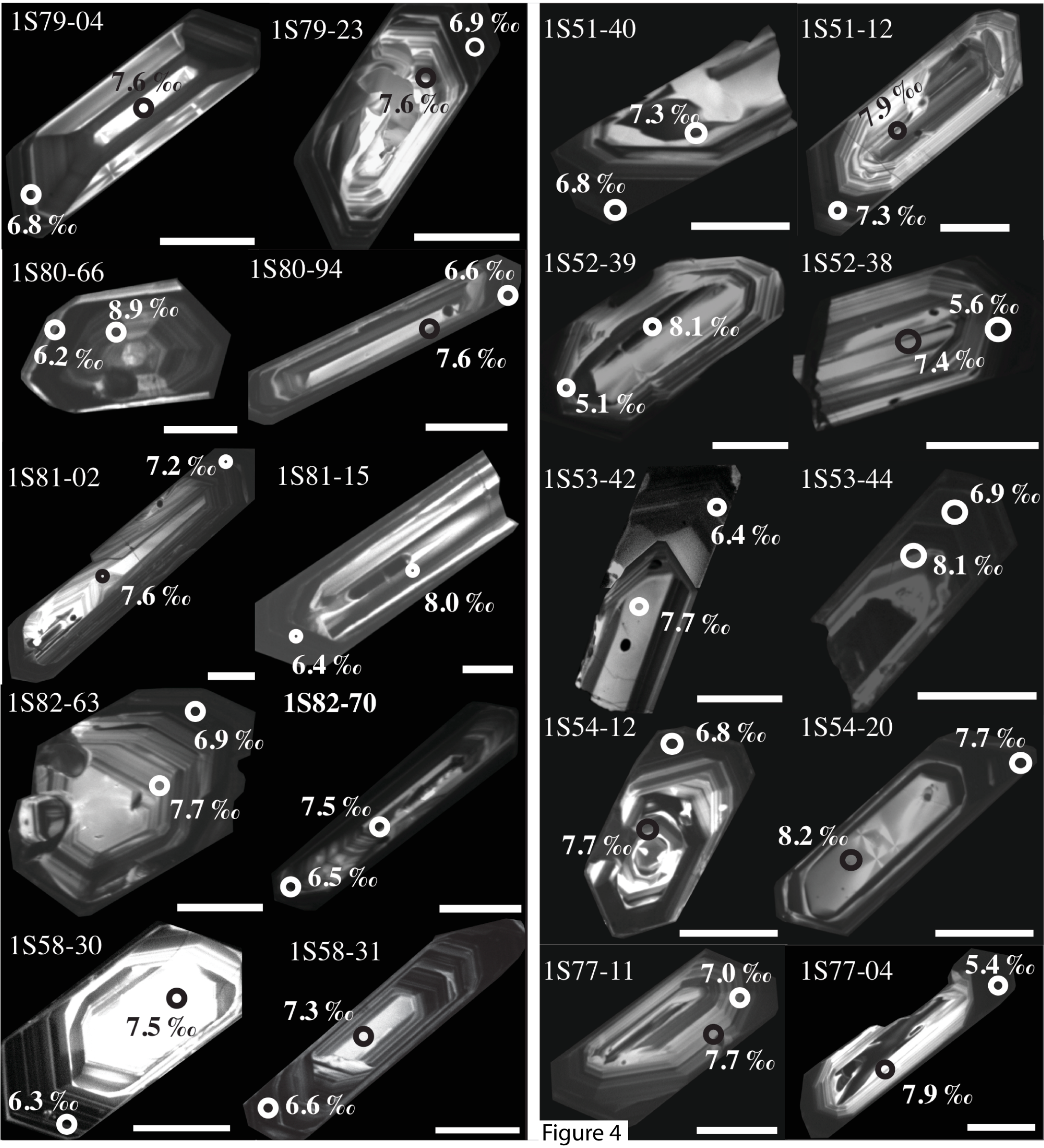
1S79-04
7.6 ‰
6.8 ‰
1S79-23
6.9 ‰
7.6 ‰
1S51-40
7.3 ‰
6.8 ‰
1S51-12
7.9 ‰
7.3 ‰
1S80-66
8.9 ‰
6.2 ‰
1S80-94
6.6 ‰
7.6 ‰
1S52-39
8.1 ‰
5.1 ‰
1S52-38
5.6 ‰
7.4 ‰
1S81-02
7.2 ‰
7.6 ‰
1S81-15
8.0 ‰
6.4 ‰
1S53-42
6.4 ‰
7.7 ‰
1S53-44
6.9 ‰
8.1 ‰
1S82-63
6.9 ‰
7.7 ‰
1S82-70
7.5 ‰
6.5 ‰
1S54-12
6.8 ‰
7.7 ‰
1S54-20
7.7 ‰
8.2 ‰
1S58-30
7.5 ‰
6.3 ‰
1S58-31
7.3 ‰
6.6 ‰
1S77-11
7.0 ‰
7.7 ‰
1S77-04
5.4 ‰
7.9 ‰

Figure 4

Figure 5

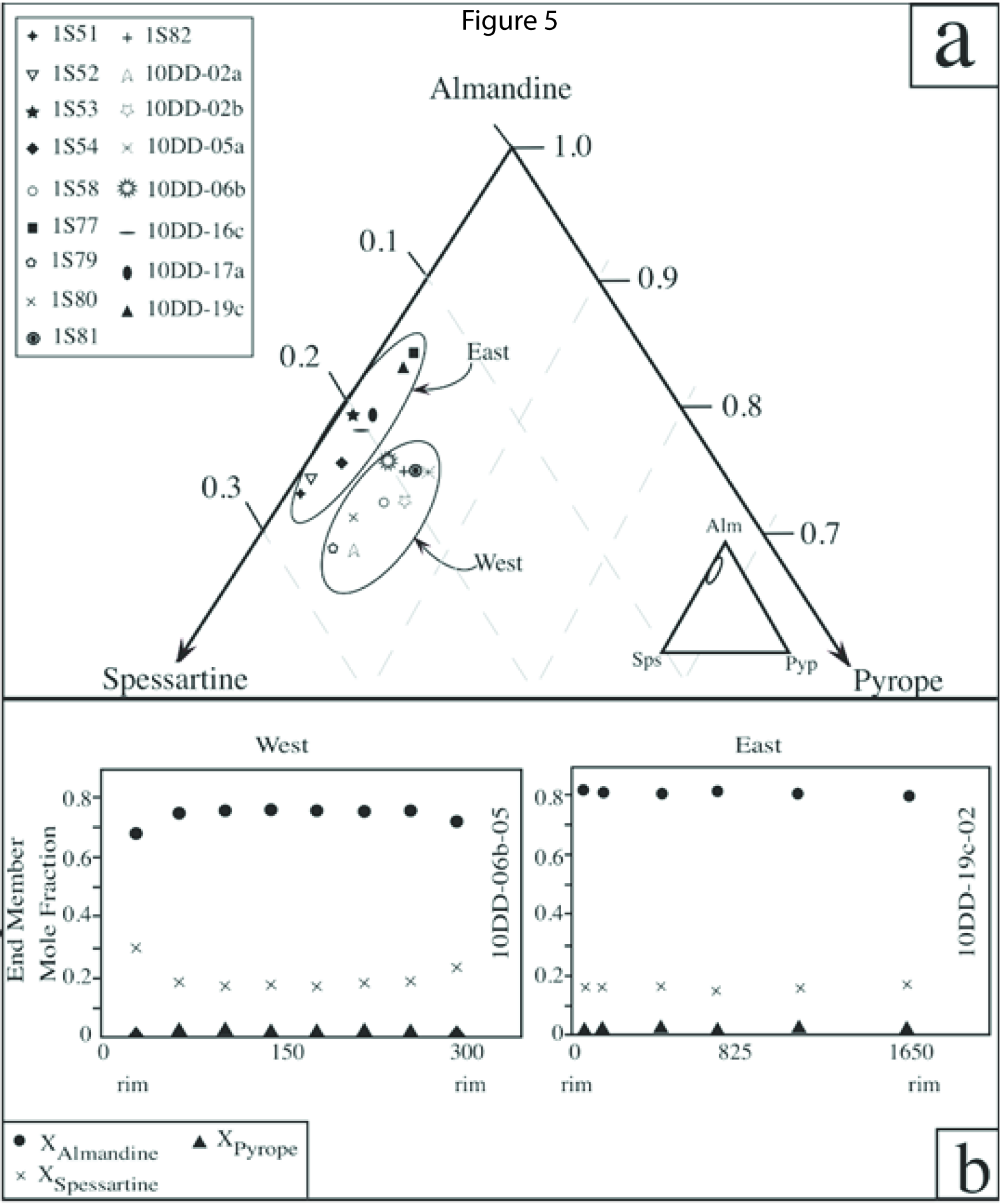

a
1S51
1S52
1S53
1S54
1S58
1S77
1S79
1S80
1S81
1S82
10DD-02a
10DD-02b
10DD-05a
10DD-06b
10DD-16c
10DD-17a
10DD-19c
Almandine
1.0
0.9
0.8
0.7
0.1
0.2
0.3
East
West
Alm
Sps
Pyp
Spessartine
Pyrope
West
East
End Member Mole Fraction
10DD-06b-05
10DD-19c-02
0
0.2
0.4
0.6
0.8
0
150
300
0
825
1650
rim
rim
rim
rim
$X_{Almandine}$
$X_{Pyrope}$
$X_{Spessartine}$
b

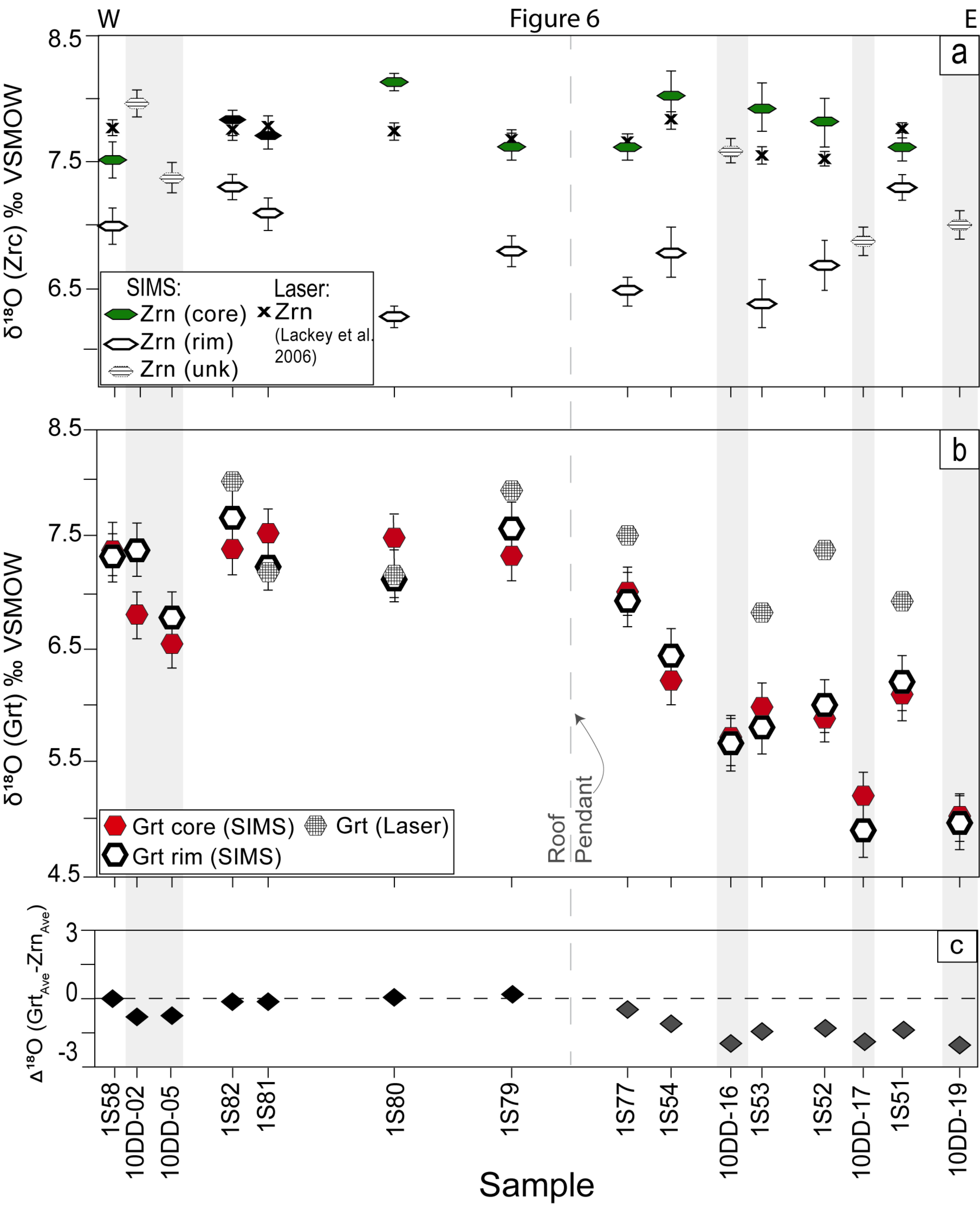

W
Figure 6
E
a
b
c
8.5
7.5
6.5
4.5
5.5
3
0
-3
δ¹⁸O (Zrc) ‰ VSMOW
δ¹⁸O (Grt) ‰ VSMOW
Δ¹⁸O (Grt_Ave-Zrn_Ave)
SIMS:
Zrn (core)
Zrn (rim)
Zrn (unk)
Laser:
Zrn
(Lackey et al. 2006)
Grt core (SIMS)
Grt (Laser)
Grt rim (SIMS)
Roof Pendant
1S58
10DD-02
10DD-05
1S82
1S81
1S80
1S79
1S77
1S54
10DD-16
1S53
1S52
10DD-17
1S51
10DD-19
Sample

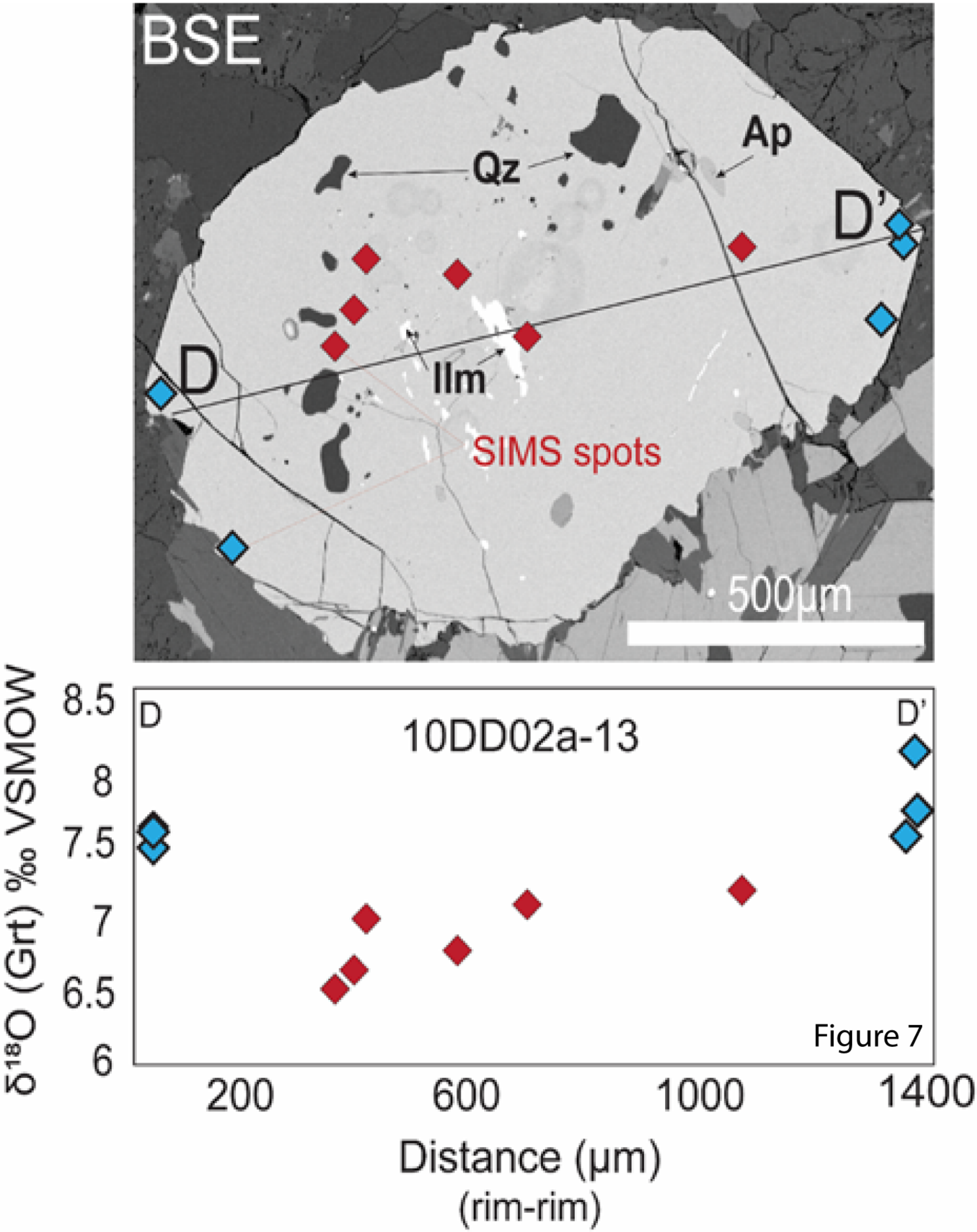
BSE
Qz
Ap
D'
D
Ilm
SIMS spots
500µm
D
D'
10DD02a-13
δ18O (Grt) ‰ VSMOW
8.5
8
7.5
7
6.5
6
200
600
1000
1400
Distance (µm)
(rim-rim)

Figure 7

# Figure 8

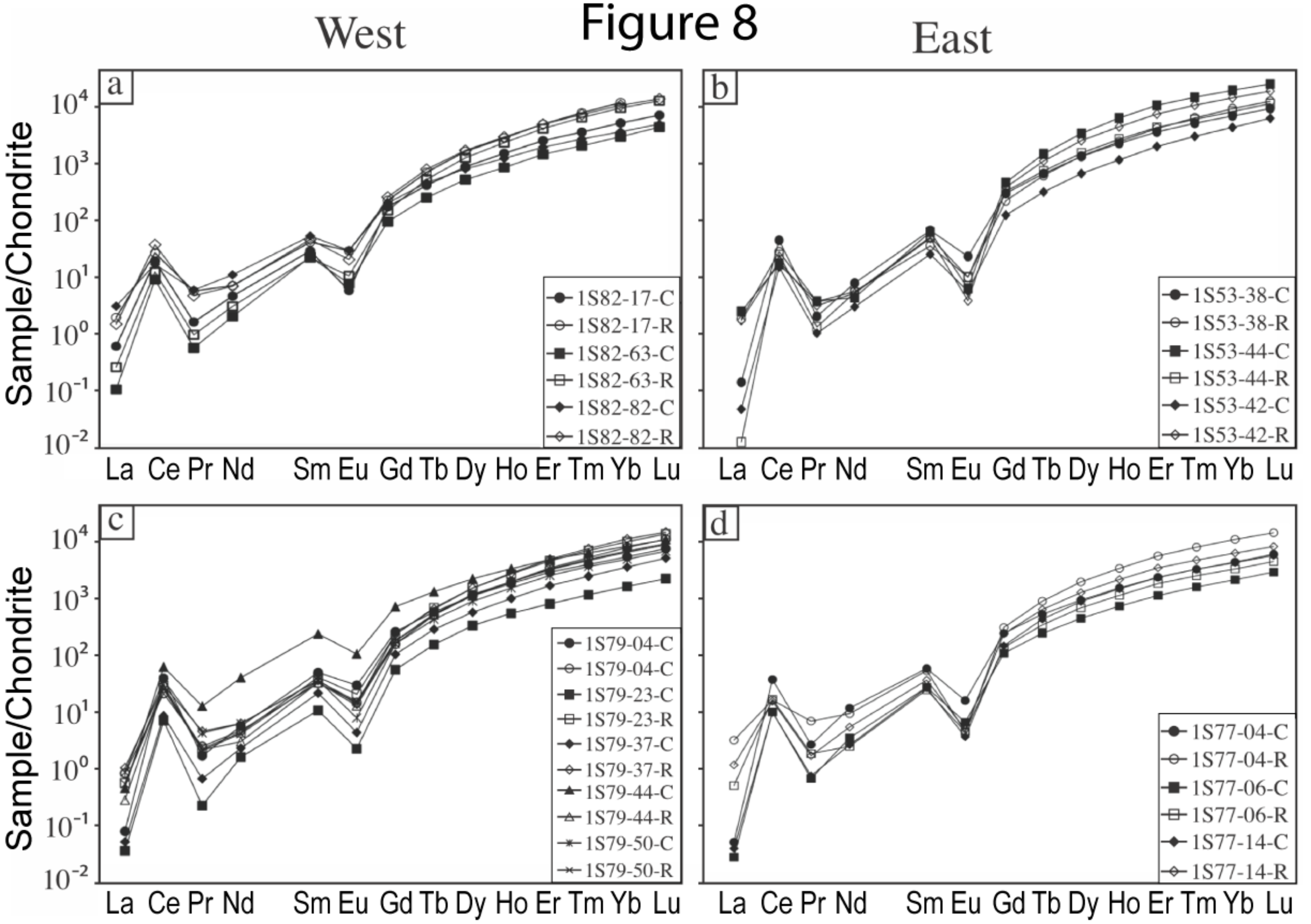
West
East
a
b
c
d
Sample/Chondrite
10^4
10^3
10^2
10^1
10^0
10^-1
10^-2
La Ce Pr Nd Sm Eu Gd Tb Dy Ho Er Tm Yb Lu
1S82-17-C
1S82-17-R
1S82-63-C
1S82-63-R
1S82-82-C
1S82-82-R
1S53-38-C
1S53-38-R
1S53-44-C
1S53-44-R
1S53-42-C
1S53-42-R
1S79-04-C
1S79-04-C
1S79-23-C
1S79-23-R
1S79-37-C
1S79-37-R
1S79-44-C
1S79-44-R
1S79-50-C
1S79-50-R
1S77-04-C
1S77-04-R
1S77-06-C
1S77-06-R
1S77-14-C
1S77-14-R

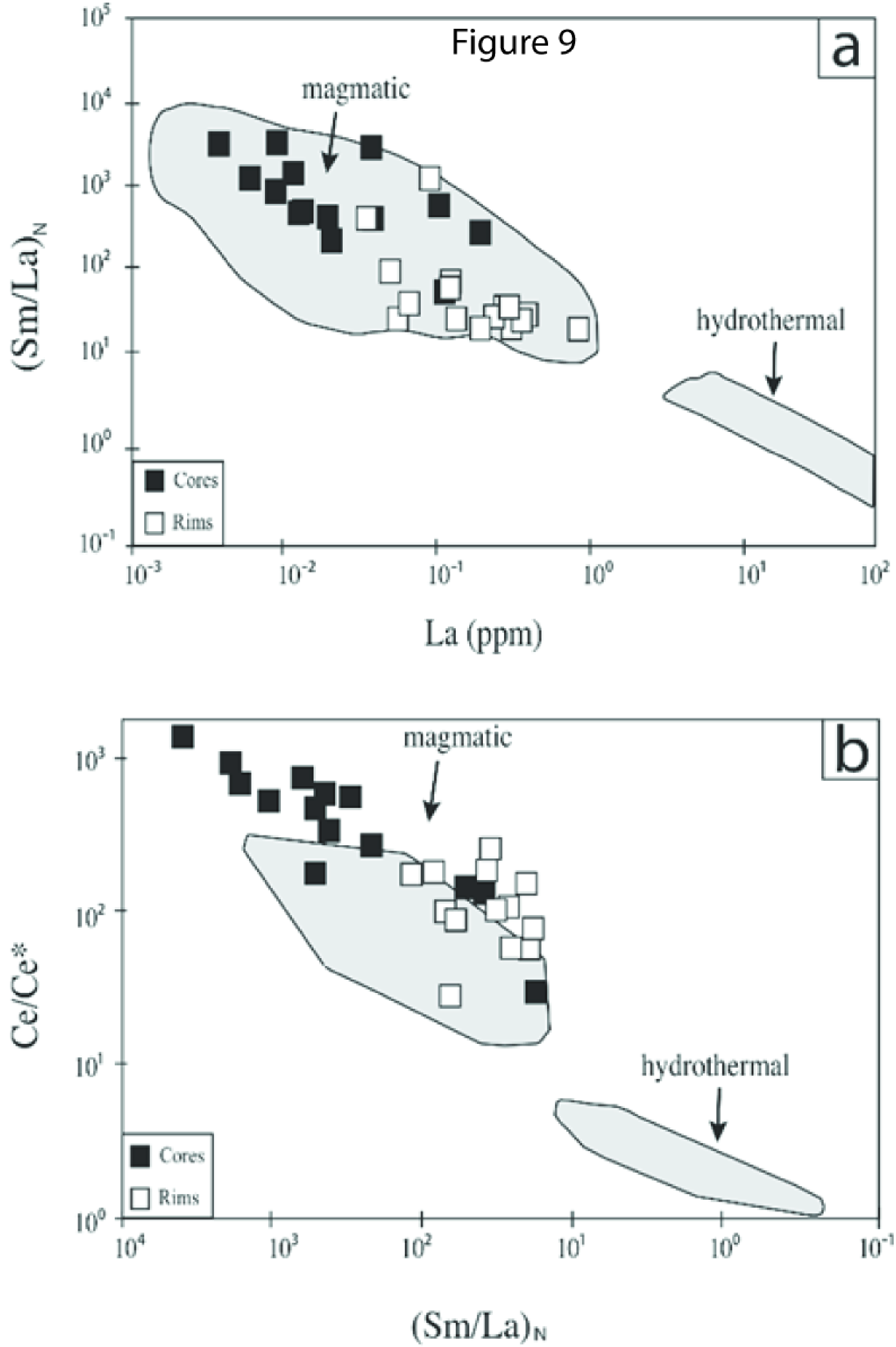
a
magmatic
hydrothermal
Cores
Rims
(Sm/La)N
La (ppm)
b
magmatic
hydrothermal
Cores
Rims
Ce/Ce*
(Sm/La)N

Figure 9

Figure 10

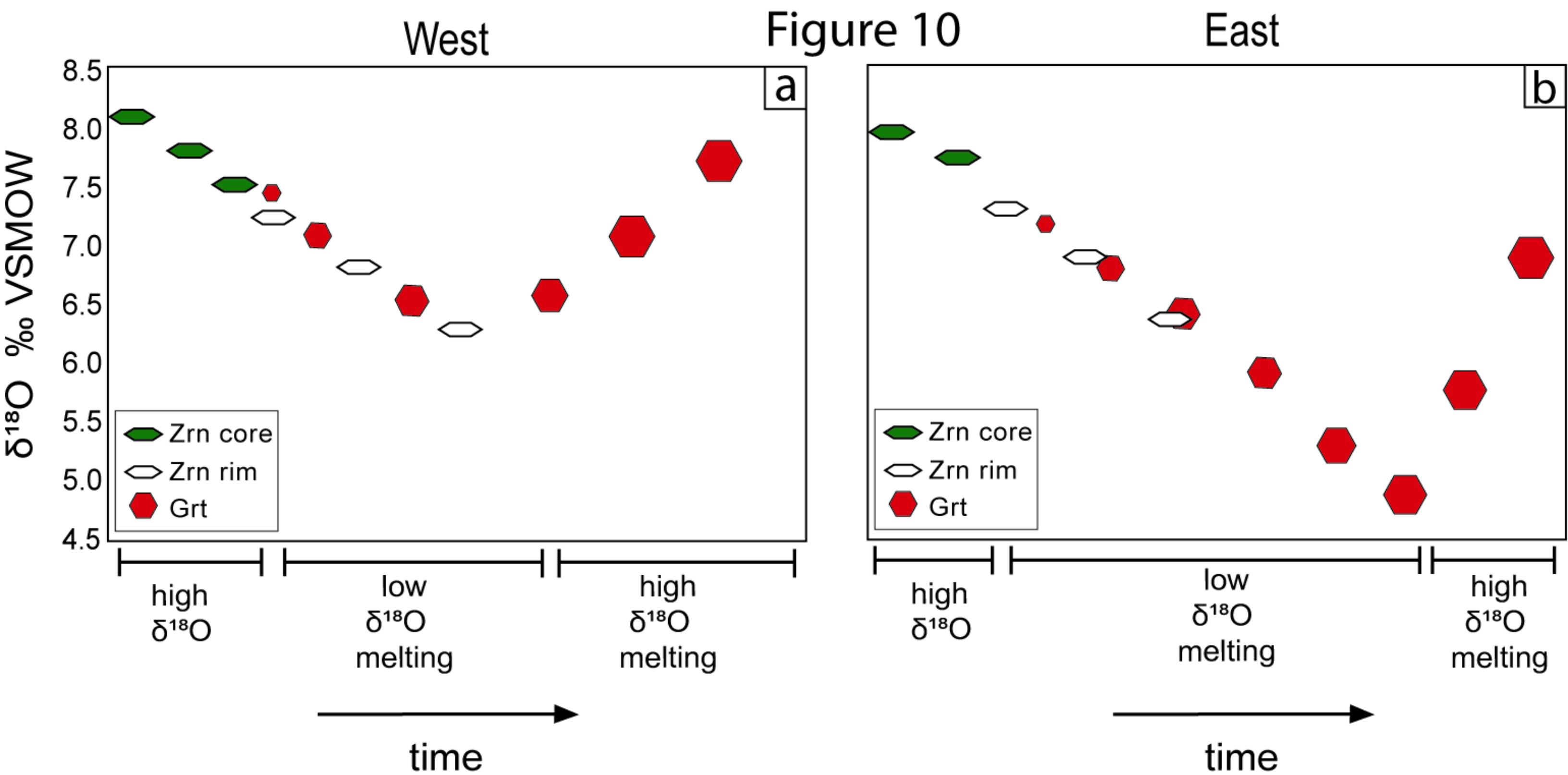

West
East
a
b
8.5
8.0
7.5
7.0
6.5
6.0
5.5
5.0
4.5
δ18O ‰ VSMOW
Zrn core
Zrn rim
Grt
high δ18O
low δ18O melting
high δ18O melting
time

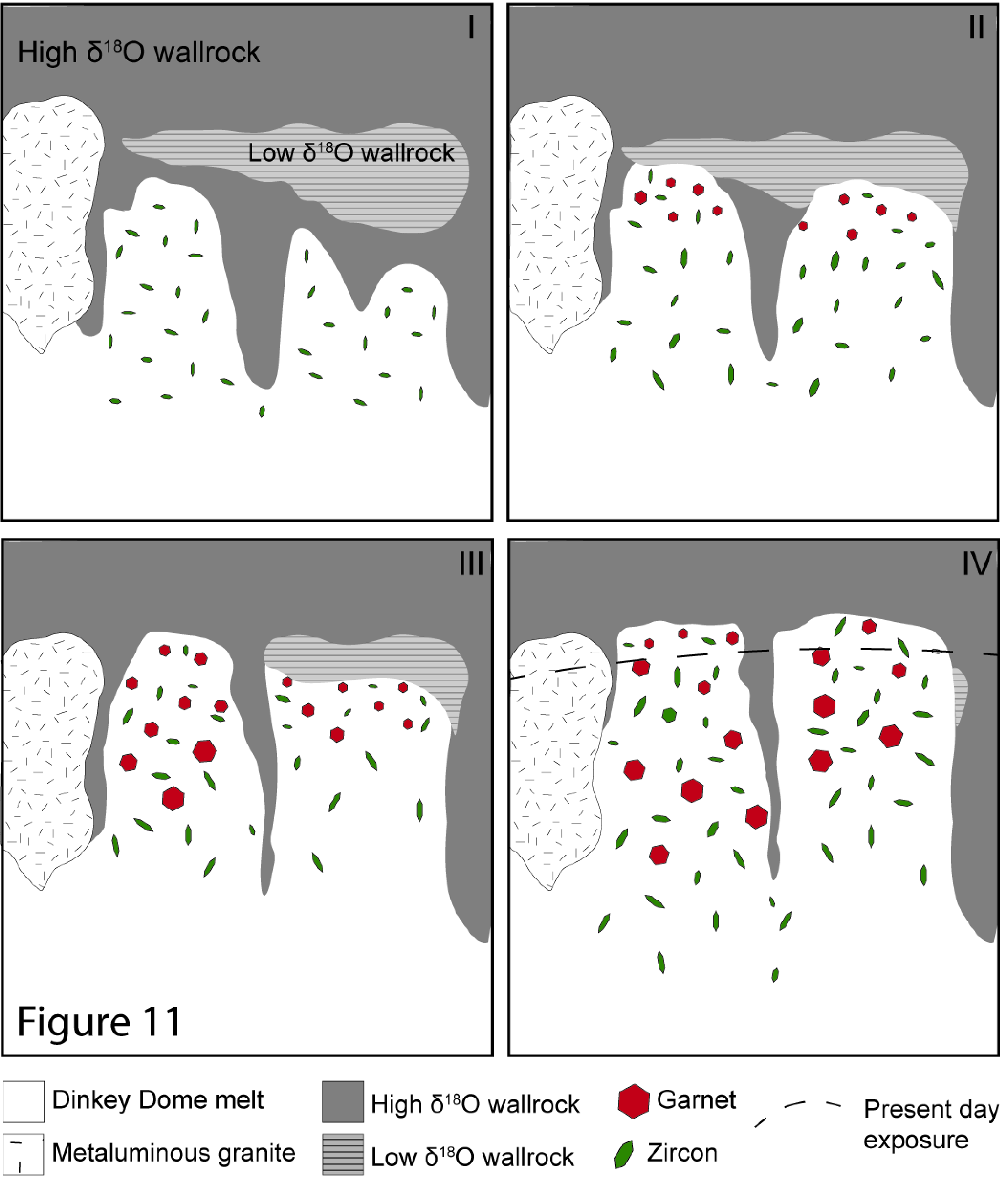

I
High δ18O wallrock
Low δ18O wallrock
II
III
IV
Dinkey Dome melt
Metaluminous granite
High δ18O wallrock
Low δ18O wallrock
Garnet
Zircon
Present day exposure


Figure 11